

Accepted for publication in *The Astrophysical Journal*

***BEPPOSAX* and *RXTE* SPECTRAL STUDY OF THE LOW-MASS X-RAY BINARY 4U 1705-44. SPECTRAL HARDENING DURING the BANANA BRANCH**

Elena Seifina¹, Lev Titarchuk², Chris Shrader^{3,4} & Nikolai Shaposhnikov^{3,5}

ABSTRACT

We analyze the X-ray spectra of the atoll 4U 1705-44 when the source undergoes the island–banana state transition. We use the *Rossi* X-ray Timing Explorer (*RXTE*) and *BeppoSAX* observations for this analysis. We demonstrate that the broad-band energy spectral distributions for all evolutionary states can be fitted by a model, consisting two Comptonized components. One arises from the seed photons coming from a neutron star (NS) atmosphere at a temperature $kT_{s1} \lesssim 1.5$ keV (herein Comptb1) and a second resulting from the seed photons of $T_{s2} \sim 1.1–1.3$ keV coming from the disk (herein Comptb2). We found that we needed to add a low-temperature blackbody and an iron-line (Gaussian) component to the model in order to obtain high–quality fits. The data analysis using this model indicates that the power-law photon index Γ_1 of our model is always about 2, independently of the spectral state. Another parameter, Γ_2 demonstrates a two-phase behavior depending on the spectral state. Γ_2 is quasi-constant at $\Gamma_2 \sim 2$ when the electron temperature $kT_e^{(2)} < 80$ keV and Γ_2 is less than 2, in the range of $1.3 < \Gamma_2 < 2$, when $kT_e^{(2)} > 80$ keV. This phase

¹Moscow State University/Sternberg Astronomical Institute, Universitetsky Prospekt 13, Moscow, 119992, Russia; seif@sai.msu.ru

²Dipartimento di Fisica, Università di Ferrara, Via Saragat 1, I-44122 Ferrara, Italy, email:titarchuk@fe.infn.it; Goddard Space Flight Center, NASA, code 663, Greenbelt MD 20770, USA; email:lev@milkyway.gsfc.nasa.gov, USA

³NASA Goddard Space Flight Center, NASA, Astrophysics Science Division, Code 661, Greenbelt, MD 20771, USA; Chris.R.Shrader@nasa.gov

⁴Universities Space Research Association, 10211 Wincopin Cir, Suite 500, Columbia, MD 21044, USA

⁵CRESST/University of Maryland, Department of Astronomy, College Park MD 20742, Goddard Space Flight Center, NASA, code 663, Greenbelt MD 20771, USA: email:nikolai.v.shaposhnikov@nasa.gov

is similar to that was previously found in the Z -source Sco X-1. We interpret the decreasing index phase using a model in which a super-Eddington radiation pressure from the neutron star causes an expansion of the Compton cloud similar to that found previously in Sco X-1 during the Flaring branch.

Subject headings: accretion, accretion disks—black hole physics—X-ray:binaries—stars: individual (4U 1705-44)—radiation mechanisms: nonthermal

1. Introduction

Low mass X-ray binaries (LMXBs), which contain a neutron star (NS), have been observationally classified as atoll-type and Z -type XBs (Hasinger & van der Klis, 1989). The distinct observational characteristics of these two groups are not fully understood. This classification was initially based on the patterns which could be traced out using the Color Color Diagram (CCD). The CCD of Z -sources shows three branches [horizontal, normal and flaring ones (HB, NB and FB respectively) or so called a Z -pattern, while the CCD of atolls displays two branches. These two branches of atolls are known in the literature as the island and the banana states. However later it has been also found that these two classes exhibit quite different spectral and timing properties.

The main difference between these two groups is probably related to their different luminosity ranges. Most atolls vary in the range from 0.01 to 0.5 of the Eddington limit L_{Edd} , while Z -sources irradiate close to L_{Edd} . Their luminosity is in the (0.5 - 1) L_{Edd} range. In this context, Lin et al. (2009) and Homan et al. (2010) made an interesting suggestion for the Z -track sources using *RXTE* observations of the transient neutron source NS XTE J1701-462. The source behaves as a Z -source when its luminosity was close to L_{Edd} , and when the source fades, it shows all properties of an *atoll*. However, the observations of XTE J1701-462 for the last seven years no longer demonstrate this type of behavior.

Another example of the hybrid atoll and Z -source properties is revealed in a unique source 4U 1705-44. It shows the spectral soft-hard state evolutions on the time scales of a month with well-determined recurrence. Also Langmeier et al. (1987); Sztajno et al. (1985) and Di Salvo et al., (2015) found type I X-ray bursts and Ford et al. (1998) discovered kilohertz quasi-periodic oscillations. While 4U 1705-44 is identified as an atoll, it also has properties of a Z -source (Barret & Olive, 2002, hereafter BO02). The power density spectra (PDS) of 4U 1705-44 resemble those of Z -sources when it is on its diagonal branch (similar to the *normal* branches of Z -sources). In this case its PDS resembles those found on the top branch of the Z -track (see the *RXTE* data analysis in BO02).

Usually a sum of a soft *blackbody* component, presumably forming in the accretion disk (AD), and a hard X-ray component originating in a corona [a transition layer (TL), located between the NS and the AD] well describes X-ray spectra of NS LMXBs . In addition, a broad iron line (most likely the Fe K emission) is often revealed. BO02 analyzed the *RXTE* PCA data of 4U 1705-44 focusing on the spectral-timing behavior. They used this model and included a 6.4 keV iron line component to show that the spectral transitions of 4U 1705-44 were followed by changes of the plasma temperature of the Comptonizing cloud. However, the BO02 model did not separate the contribution of the Comptonized disk photons from that of the NS photons in the resulting spectrum. Paizis et al. (2006) and Fiocchi et al. (2007) presented the average INTEGRAL IBIS spectrum of 4U 1705-44 which indicated the existence of a high-energy tail in the spectrum.

Recently Seifina et al (2013), hereafter STF13, applied a so-called two component Comptonization model to the spectral data of GX 340+0 and Titarchuk et al. (2014, hereafter TSS14), analyzed the data of Sco X-1 using the same model. Note that GX 340+0 and Sco X-1 are *Z*-sources. This self-consistent model allows one to separate Comptonized emission caused by upscattering of the NS surface photons in a Compton cloud from that caused by the seed photons of the accretion disk. STF13 demonstrated that the Comptonized emission of the NS photons dominates during all spectral states for GX 340+0 and Sco X-1, while that related to the Comptonized disk photons formed the hard energy tail of X-ray spectrum. Previously, Farinelli et al. (2009) successfully implemented the same kind of model in an analysis of the *BeppoSAX* observations of *Z*-source Cyg X-2 to describe the spectral evolution of the source from the HB to the NB.

The broad-band (0.1 – 200 keV) spectrum of 4U 1705-44 was analyzed by Egron et al. (2013), who used the combined data of *BeppoSAX*, *XMM-Newton*, and *RXTE*. The authors fitted the spectrum by a combination of a BB plus a thermal Comptonized model (**compTT** or **nthcomp**, in the XSPEC package), modified by the photoelectric absorption (*phabs*) at low energies. Their fit was modified by the addition of a broad **Gaussian** line and also by inclusion of the reflection components **pexriv** or **reflionx**. Their results are in agreement with those reported by Piraino et al. (2007) and Di Salvo et al. (2009) for the soft state of 4U 1705-44. In particular, these authors found that in the soft state, N_H varies from 1.96×10^{22} cm $^{-2}$ to 3.64×10^{22} cm $^{-2}$ and the index Γ changes from 2.2 to 2.6, the BB temperature is about 0.5 keV, the plasma and seed photon temperatures of the Comptonized component are 3.5 keV and 1.2 keV, respectively. The centroid energies of four *line* components are at 2.6 keV, 3.31 ± 0.03 keV, 3.88 ± 0.03 keV and 6.63 ± 0.01 keV, respectively. Egron et al. (2013) used a similar model to fit the hard state spectra of 4U 1705-44. They found that in the hard state N_H is about 2.0×10^{22} cm $^{-2}$, the index Γ changes from 1.8 to 2.0, the BB temperature ranges from 0.24 keV to 0.58 keV, and the electron and seed photon

temperatures of the Comptonized component are about 21 keV and 0.7 keV, respectively. The inclination of the system, estimated using the `diskline` or the reflection component, is in the interval of $30^\circ - 40^\circ$ [see Egron et al. (2013); D’Ai et al. (2010); Di Salvo et al. (2009) and Di Salvo et al. (2015)]. Note that XMM-*Newton* data analysis done by Egron et al. (2013) provides a value N_H around $2 \times 10^{22} \text{ cm}^{-2}$ for both of the hard and soft states. They also find that the N_H value derived from the non-simultaneous *RXTE* data is different, $N_H = (3.64 \pm 0.02) \times 10^{22} \text{ cm}^{-2}$.

Recently, Church et al. (2014) present the relation between atoll and *Z*-sources in the frame of a unified model for LMXBs. Based on the *RXTE* and *BeppoSAX* data analysis for a number of *Z* and atoll sources (4U 1705-44 among them) they used the so-called ADC (the Comptonizing accretion disk corona) model to show how the ISs and BSs in atolls relate the states seen in *Z* sources. Particularly, they demonstrated a common feature of *Z* and atoll behavior of the electron temperature T_e being high in the hard states and then it sharply dropping at the “critical” luminosity of about $2 \times 10^{37} \text{ erg s}^{-1}$. But T_e is low (at about $T_e \sim T_{BB}$) when the luminosity increases during the soft states.

Church et al. (2014) also claim that the IS of atoll sources is characterized by a high T_e based on the ADC model but the IS is absent in *Z*-sources because their luminosities are greater than a “critical” value. Also in *Z*-sources there is the flaring Branch (FB) which is associated with unstable nuclear burning on the NS at high mass accretion rate \dot{M} . This unstable burning regime is not pronounced at low \dot{M} and thus this branch is not observed in atoll sources (except in the GX atolls). However, Church et al. (2014) are not able to explain the presence of a high energy tail seen up to 200 keV in *Z*-sources (D’Ai et al. 2007) and in the soft state of atoll-sources. In particular, Di Salvo et al. (2000) discovered a state-dependent hard energy tail in *Z*-source GX 17+2. For example, the prominent tail in Sco X-1 was first revealed by D’Amico et al. (2001) with HEXTE/*RXTE* and Di Salvo et al. (2006) using *BeppoSAX*. The first *hard tail* in *atoll*-type source was discovered by Piraino et al. (2007). Thus, it is necessary to take into account these high-energy tails in analyzing the spectra of atoll and *Z* sources.

TSS14 studied the spectral-timing property relations observed in Sco X-1 using the *RXTE* observations. They found that the Sco X-1 energy spectra [for (3–200) keV range] during all *Z*-state transitions could be adequately reproduced by a double-Comptonization model. This model allows us to separate two contributions to the resulting spectrum. One spectral component is presumably associated with the Comptonization of the NS seed photons and another one is related to the Comptonization of the seed photons from the disk. Using this model, TSS14 reveal a unique stability of Γ_1 and Γ_2 which values are around 2 during the *Z*-states except of the FB. TSS14 explain the detected stability of these photon

indices using the model in which the disk photon flux is negligibly small with respect to the energy release in the TL. However, over the FB TSS14 detect the decreasing index phase, which they interpret using a model in which the accreted matter deposits its gravitational energy only in some external part of the TL. In this case the TL innermost part is cooler than the outer part (mostly owing to illumination by the NS soft photons), and thus the resulting radiative luminosity L_r achieves the Eddington one there. As a result, the accretion flow is stopped by $L_{r,\text{Edd}}$.

In this paper we analyze the *BeppoSAX* observations of 4U 1705-44 that took place during August and October of 2000 [see Fiacchi et al. (2007), Piraino et al. (2007), Egron et al. (2013)]. We also analyze the *RXTE* observations that were made during 1997 – 2000 [see Barret & Olive (2002), Munro et al. (2002) and Egron et al. (2013)] In §2 we present the details of our data selection procedure and show an observation list that we selected for our analysis. In §3 we give the spectral analysis details. We interpret the spectral properties and their evolution observed during the different spectral states in §4. Our results are discussed and our conclusions are presented in §5.

2. Data Selection

In 2000 August and October *BeppoSAX* observed 4U 1705-44 (see details in Table 1). A combination of the data from three *BeppoSAX* instruments gives us the source energy spectra. Namely, we used Narrow Field Instruments (NFIs): the Low Energy Concentrator Spectrometer (LECS; Parmar et al. (1997)) for the 0.3 – 4 keV range, the Medium Energy Concentrator Spectrometer (MECS; Boella et al. (1997)) for the 1.8–10 keV range, the High Pressure Proportional Gas Scintillation Counter (Manzo et al. 1997) for the 8–50 keV range, and the Phoswich Detection System (Frontera et al. 1997) for the 15–150 keV range.

For data reprocessing we applied the SAXDAS data analysis package and we carried out the spectral analysis in the energy band related to each of these instruments. A relative NFI normalization was considered as a free parameter for the model fitting. However, we fixed the MECS normalization at 1. Following this procedure, we wanted to control that all of these normalizations were located in standard instrument ranges ¹.

We also rebinned the spectra to obtain significant data points. In particular, the LECS spectra were rebinned with a binning factor which is not constant over energy (see §3.1.6 of Cookbook for the *BeppoSAX* NFI spectral analysis). For this rebinning we applied template

¹<http://heasarc.nasa.gov/docs/sax/abc/saxabc/saxabc.html>

files in GRPPHA of XSPEC ². Moreover, the Phoswich Detection System spectra were rebinned with a binning factor of 2 when we grouped two bins together (resulting width of the bin is 1 keV). We applied a systematic error of 1% to *BeppoSAX* spectra. We list all *BeppoSAX* observations used in the presented analysis in Table 1.

We have also used the *RXTE* data which were obtained from 1997 April to 2000 February. In total, these data include 86 observations sampling the different spectral states. For data processing we utilized standard tasks of the LHEASOFT/FTOOLS 5.3 software package. We applied Proportional Counter Array (PCA) Standard 2 mode data, accumulated in the 3–23 keV energy range, using the most recent release of PCA response calibration (ftool pcarmf v11.7) for a spectral analysis. We also applied a standard dead time correction procedure to the data. To construct broadband spectra, the data from HEXTE detectors were used. A background derived from off-source observations was subtracted from the source signal.

We have included only data in the 19–200 keV range. Thus, we accounted for the HEXTE response uncertainties and determination of the background. The data are available through the GSFC public archive (<http://heasarc.gsfc.nasa.gov>). A list of observations that covers the source spectral evolution is present in Table 2.

In Figure 1 we plot the overall light curve of the All Sky Monitor (ASM; Levine et al. 1996) on board *RXTE* in order to assess the intensity of the source on long timescales. The ASM data (from 1995 October 10 to 2002 August 14 2002) indicate long-term variability on the scale of 1 month from 5 ASM counts s^{-1} (corresponding to the hard state) to 35 ASM counts s^{-1} (the soft state). Note that during the hard state a type-I X-ray burst occurred, but none occurred in the soft state (see D’Ai et al., 2010). In fact, we have excluded the type I bursts from the analysis. Generally, the source showed the hard-to-soft transitions characterized by the different timescales of the X-ray flux variability. As seen from Fig. 1, we have chosen the time intervals with long (with high flux “plateau”, *R1* set) and with relatively shorter timescale periods of variability (*R2* and *R3*). Thus, we have made a *RXTE* analysis of the 4U 1705-44 data for 3 yr of observations and divided them to three intervals indicated by blue rectangles in Figure 1 (*top*). The *RXTE* energy spectra were modeled using XSPEC astrophysical fitting software. We applied a systematic uncertainty of 0.5% to all analyzed *RXTE* spectra.

²<http://heasarc.gsfc.nasa.gov/FTP/sax/cal/responses/grouping>

3. Results

3.1. CCDs diagrams of 4U 1705-44

To investigate the properties of 4U 1705-44 during different spectral states, we use hard colors (HCs) and soft colors (SCs) and we demonstrate different configurations of CCDs (CCDs, HC versus SC). In Figure 2 we combined CCDs (left panel) and hardness-intensity diagrams (HIDs; right panel). The axes of CCDs show the flux ratios, $[20-40 \text{ keV}/9-20 \text{ keV}]$ and $[4-9 \text{ keV}/2-4 \text{ keV}]$, while HIDs demonstrate flux ratios, $[20-40 \text{ keV}/9-20 \text{ keV}]$ versus PCA count rate (2-40 keV). In the top right corner we indicate IDs of used observational sets. One can see that our data sets cover different parts of HID and CCD from ISs to BSs. Therefore, we select observations performed at different flux levels in the hard and soft states and proceed to use these data for a detailed spectral analysis of the properties of 4U 1705-44 during its island–banana state evolution.

Note that the shape of the track described above, particularly in the HID, can be affected by secular shifts, the so-called parallel tracks (see, e.g. Di Salvo et al. 2003). Therefore, the data of different sets were marked by different colors (see Figure 2). While data sets investigated by us are associated with different epochs it is clear from this figure that our selected data do not show a noticeable effect of secular shifts. In particular, the HIDs exhibit plain and smooth tracks. Furthermore, we test this effect using flux units instead of counts, in which case the corresponding tracks (hardness-flux diagrams, see Sect. 3.2.4 and Fig. 3) also form a plain and smooth track.

3.2. Spectral Analysis

3.2.1. Choice of a Spectral Model

Many authors have used various models for fitting the 4U 1705-44 spectra. The hard component observed at high luminosity (the high/soft state) can be presented by a power-law that can be interpreted as Comptonization of electrons that have a nonthermal velocity distribution. Specifically, Eggen et al. (2013) fit *BeppoSAX*, *XMM–Newton*, and *RXTE* spectra related to the soft and hard states using a model which includes a Comptonization component, a soft BB component and a smeared reflection component. In particular, the latter component is used to fit the data associated with the hard state. A hard power-law component should also be added in the soft state to account for the state–dependent hard tail (see Piraino et al. 2007). Our approach is to employ a single model that is capable of representing both the hard and soft spectral states of the system with a minimal number of

free parameters, with the goal of probing the underlying physical process driving the system.

To probe our modeling approach, we proceeded initially using a model that is a sum of a Comptonization component, soft BB, and power-law, modified by an interstellar absorption. We also add a Gaussian line component to take into account a broad iron line associated with the Fe K emission. But this model [$wabs * (bbody + powerlaw + comptb + Gauss)$] provides satisfactory fits only for the soft state data [e.g., 40034-01-02-06 and 40034-01-02-09 spectra, $\chi^2_{red}=1.16$ and 1.34 [77 degree of freedom (d.o.f.), respectively, see Table 3]; in other words, the model gives a good data description only in 50% of cases. Moreover, the model requires a very large photon index (much greater than 3) for the soft-state spectra (e.g., for 40034-01-02-09 spectrum $\Gamma_{pow}=3.97\pm0.05$, see Table 3) and it gives unacceptable fits for the hard-state data [e.g., for 21292002 spectrum of *BeppoSAX* data $\chi^2_{red}=3.28$ (193 d.o.f.)] and for 40034-01-07-02G spectrum of *RXTE* data [$\chi^2_{red}=1.78$ (79 d.o.f.)]. Thus, we conclude that the best representation of the data requires a spectral model that can account for both the soft and the hard components, where each component can be represented by a Comptonization model. We use a sum of two Comptonization components, in which the first and second components are related to the soft and hard components of the spectrum respectively. As a result, the best fits of the hard- and soft-state spectra have been produced by implementation of the so-called *double Comptonization model* (using **Comptb**³ as an example of the Comptonizing model). This model consists of two Comptonized components (both due to the presence of the TL that upscatters seed photons of $T_{s1} \leq 1.7$ keV coming from the neutron star (first component *Comptb1*), and seed photons of temperature $T_{s2} \leq 1.3$ keV coming from the disk (second component *Comptb2*), a soft BB and the iron-line (Gaussian) component (see Table 3 for comparative analysis of *BeppoSAX* and *RXTE* data). Thus, we apply the double-Comptonization model for fitting all extracted spectra.

This model supports a scenario in which a Keplerian disk is detached from the *Neutron star* (NS) by the TL [see Titarchuk et al. (1998)]. In Figure 4 this spectral model is schematically illustrated. We assume that accretion into a NS occurs when the plasma goes through an AD [standard Shakura-Sunyaev disk, see Shakura & Sunyaev (1973)] and the TL. In this scenario the soft NS and disk photons are Comptonized by corona (TL) electrons. As a result, the emergent spectrum is produced in the TL, where soft photons of the temperature T_{s1} from the NS surface and thermal disk seed photons of the temperature T_{s2} are Comptonized off the relatively hot plasma (electrons) of the TL. The TL forms two Comptonized components *Comptb1* and *Comptb2*, respectively. Note that the Earth observer can see directly some fraction of the NS and disk seed photons. That motivates us to add a

³Comptb XSPEC model, see XSPEC v. 12.8.0
in <http://heasarc.gsfc.nasa.gov/docs/xanadu/xspec/models/index.html>

BB component with temperature T_{BB} to the resulting spectrum. In Figure 4 we show the soft (seed) and hard (upscattered) photons, as red and blue photon trajectories respectively.

It is worth noting that in the framework of the Comptb the emergent spectrum is a convolution of the BB spectrum of the photon temperature T_s and a normalization N_{com} with the upscattering Green function. The normalization N_{Com} , identical to the XSPEC *bbody* model:

$$N_{Com} = \left(\frac{L}{10^{39} \text{erg/s}} \right) \left(\frac{10 \text{ kpc}}{D} \right)^2. \quad (1)$$

where L is the soft photon (BB) luminosity and D is the distance to the source.

To fit the data, we apply our spectral model $wabs * (Bbody + Comptb1 + Comptb2 + Gauss)$, where the fit model parameters are the hydrogen equivalent absorption column N_H ; the energy indices α_1, α_2 ($\alpha_1 = \Gamma_1 - 1$ and $\alpha_2 = \Gamma_2 - 1$); the *seed* photon temperatures T_{s1}, T_{s2} ; parameters $\log(A_1)$ and $\log(A_2)$ related to the upscattering photon fractions f_1, f_2 , specifically where $f = A/(1 + A)$ is the relative weight of the upscattering component; the plasma (electron) temperatures $T_e^{(1)}$ and $T_e^{(2)}$, the BB normalizations N_{Com1} and N_{Com2} of the Comptb1 and Comptb2 respectively. Finally, to fit the data in the 6–8 keV range, we add a Gaussian component that is characterized by the parameters E_{line} (a centroid line energy), σ_{line} (the line width) and N_{line} (the line normalization).

In any case of $\log(A) \gg 1$ a fraction $f = A/(1 + A)$ approaches unity and thus we always fix values of $\log A_{1,2}$ at 2.

3.2.2. BeppoSAX data analysis

Using *BeppoSAX* data we demonstrate two EF_E spectral diagrams for banana and island branch events along with the atoll track presented in Fig. 5. We show the best-fit EF_E spectral diagrams of 4U 1705-44 using *BeppoSAX* observations 212921001 (left panel) and 21292002 (right panel). We indicate the data by crosses and the best-fit spectral model (see details above) by a light-blue line. Red, green, dark-blue and crimson lines are for Comptb1, Comptb2, Blackbody and Gaussian components, respectively. We present $\Delta\chi$ vs photon energy in keV in the bottom panel. For the banana (left panel) $\Gamma_1=1.99\pm0.02$, $kT_e^{(1)}=2.47\pm0.01$ keV, $\Gamma_2=2.00\pm0.01$, $kT_e^{(2)}=46.0\pm0.7$ keV, $kT_{BB} = 0.50 \pm 0.01$ keV and $E_{line}=6.50\pm0.03$ keV (reduced $\chi_{red}^2=1.12$ for 132 dof), while for the island (right panel) $\Gamma_1=2.00\pm0.01$, $kT_e^{(1)}=18.9\pm0.1$ keV, $\Gamma_2=2.01\pm0.01$, $kT_e^{(2)}=51.0\pm0.9$ keV, $kT_{BB} = 0.54 \pm 0.02$ keV and $E_{line}=6.51\pm0.07$ keV (reduced $\chi_{red}^2=1.08$ for 133 dof., see details in Table 3). The BB temperature kT_{BB} , independently of the state, is around 0.6 keV (2σ upper limit). The fit quality of the *BeppoSAX* spectra is significantly improved by inclusion of this

component. We also find that in the soft state (ObsId=21292001) N_H is a larger, namely $N_H = (2.43 \pm 0.03) \times 10^{22} \text{ cm}^{-2}$ versus that in the hard state (ObsId = 21292002) for which $N_H = (2.16 \pm 0.04) \times 10^{22} \text{ cm}^{-2}$.

Using our model we find that the photon indices of the *BeppoSAX* spectra $\Gamma_{1,2} = \alpha_{1,2} + 1$ are 2.02 ± 0.02 and 2.01 ± 0.01 correspondingly (see Table 3). We also find that the seed temperatures kT_{s1} and kT_{s2} vary in the ranges 1.4–1.5 keV and 1.1–1.3 keV, respectively.

3.2.3. *RXTE data analysis*

The *RXTE* spectra below 3 keV are not well calibrated; however one can use the BB component parameters using the *BeppoSAX* broad energy band (0.1–200 keV). Thus, in order to fit the *RXTE* data we have fixed the *BB* temperature of the (inner disk) component at $kT_{BB} = 0.6$ keV found from our analysis of the *BeppoSAX* data. Furthermore, because of the limited PCA low-energy coverage, we let N_H be free and constrained to lie in the range $2 - 4 \times 10^{22} \text{ cm}^{-2}$ as early reported by different authors (see e. g. Di Salvo et al. 2005, 2009; D’Ai et al. 20012; Egron et al. 2013). In Table 4 we present the best-fit spectral parameters using the two-Comptb model applied to the *RXTE* observations.

We obtain that N_{Com1} varies from 0.01 to 6.1 in units of L_{37}/D_{10}^2 (L_{37} is the seed photon blackbody luminosity in units $10^{37} \text{ erg s}^{-1}$ while D_{10} is distance in units of 10 kpc). The index Γ_1 is almost constant ($\Gamma_1 = 1.99 \pm 0.06$) for all observations (see Fig. 6). We reveal a two-phase behavior for the photon index Γ_2 : the phase of the quasi-constant photon index ($\Gamma_2 = 2.01 \pm 0.07$) when $kT_e^{(2)}$ varies between 3 keV and 85 keV, and the phase of the reduced photon index ($\Gamma_2 < 2$) for the high electron temperature $kT_e^{(2)} > 85$ keV (see Fig. 6, right diagram). Note that the *Gaussian* component width σ_{line} does not significantly change and numerous tests show that it lies in the range of 0.5–0.8 keV. D’Ai et al. (2010), Di Salvo et al. (2001), Fiocchi et al. (2007) and Egron et al. (2013) carried out a detailed analysis of the *XMM-Newton* spectra of 4U 1705-44 and they concluded that the iron line is quite broad during all spectral states. Therefore, we chose to fix σ_{line} at a value 0.7 keV for all our fits. The electron temperatures $kT_e^{(1)}$ and $kT_e^{(2)}$ change in wide ranges from 3 to 20 keV and from 3 to 100 keV respectively (see Figure 6).

3.2.4. *Hardness–Flux Diagrams of 4U 1705-44*

The hardness–flux behavior depends on the energy bands. Figure 3 demonstrates the different shapes of the atoll tracks of 4U 1705-44 depending on the energy band (in flux

units). In all these diagrams we use the same observations but divided into different energy bands. Specifically, we plot the flux ratio $[10\text{-}50\text{ keV}/3\text{-}10\text{ keV}]$ versus flux in $[3\text{-}10\text{ keV}]$ (left), $[10\text{-}50\text{ keV}]$ (center) and $[50\text{-}200\text{ keV}]$ (right) ranges measured in units of $10^{-9}\text{ erg s}^{-1}\text{cm}^{-2}$. To make these diagrams, we apply our double Comptb spectral model.

We found that the source exhibited two color states, namely, in the IS and the BS. Here, the black arrow (left panel) indicates the direction of state changing from the island to the banana, whereas green arrow (center panel) marks the direction of state changing from the banana to the island. Note that this hysteresis effect has already been pointed out by BO02 for ID=20074 and 40051 sets. Previously, Gierlinski & Done (2002) also revealed a Z-shape of CCD track for 4U 1705-44.

While the atoll-track for 4U 1705-44 resembles a “C”-track, the source really moves in a more complicated manner resembling a Z-track. In fact, 4U 1705-44 is characterized by an extreme IS, particularly well seen as an upper elongated horizontal branch in the *central* panel. However this branch is not seen on the left panel (for a softer flux case). Thus, the source behaves as a Z-source in terms of hardness-flux track.

Note that the hard emission events are accompanied by a decrease of radio emission as observed in a number of Z-sources [Hjellming et al. (1990)]. However, 4U 1705-44 is not seen at radio wavelengths so far (see Fender & Hendry 2000). Furthermore, in agreement with previous timing analysis, 4U 1705-44 demonstrates the typical timing properties of atoll sources. But we should point out the unusual CCD/HID track of this standard atoll source, which is reminiscent of a Z-shape in its hardness-flux diagram. This effect is essentially caused by its elongated extreme IS which is rarely observed from atoll sources.

3.3. Overall pattern of X-ray properties

We have found that 4U 1705-44 was in four different spectral states, each of which is represented by EF_E spectral diagrams are shown in Figure 7. Data (shown by black crosses) are taken from *RXTE* observations 40034-01-09-00 (IS), 40034-01-01-00 (lower left banana, LLB), 40034-01-02-09 (lower banana, LB), and 40034-01-02-06 (*upper banana*, UB). We show the spectral model components by dashed red, green, blue and purple lines for Comptb1, Comptb2, BB and Gaussian, respectively. To demonstrate an evolution of Comptb2 between the IS, LLB, LB and UB branches, we use yellow shaded areas. Here we show spectral changes in the energies greater than 30 keV that reflect the contribution of the Comptonized components (Comptb1 and Comptb2) for different atoll branches. In Figure 8 we also illustrate these spectral changes using the plot of the electron temperature

kT_e versus the hard luminosity (for 10–50 keV energy range) along the total atoll cycle of 4U 1705–44.

The relative softening of the Comptb2 component shown in the LB panel in comparison with that presented in the IS, LLB and UB panels is seen in Fig. 7. On the other hand, the UB panel shows the hardening of the spectrum at high energies, the photon index $\Gamma_2 < 2$ in this case. The hard emission at 50–150 keV (high-energy tail) becomes stronger along the UB, in comparison of that for the IS and LLB (when $\Gamma_2 \sim 2$). In our data set we have found five observations (20161-01-02-00, 20161-01-02-01, 40034-01-02-06, 40034-01-05-07, 40051-03-03-00) in which the high energy tail is strong and extended to 200 keV (similar to that presented in the right panel of Fig. 7). In all these cases the photon index of the *hard* Comptonized component corresponds to reduced values $\Gamma_2 < 2$. In Fig. 6 we combine these points with $\Gamma_2 < 2$ for $kT_e > 80$ keV with the nearly constant plateau of $\Gamma_2 \sim 2$ for $kT_e < 80$ keV.

To understand what are the possible reasons that can cause the above–mentioned hardening of the 4U 1705–44 spectrum at UB, we plot the photon indices Γ_1 and Γ_2 vs. the seed photon temperatures T_{s1} and T_{s2} (see Fig. 9). Red and blue points correspond to Comptb1 and Comptb2, respectively and thus one can clearly distinguish the Comptonization of soft photons of the NS surface and that related to disk photons in the TL. As is seen from this plot, Γ_2 is less than 2 when the kT_{s2} monotonically drops from 1.3 keV to 1.1 keV. This is the first indication that the index drops when the area of the TL increases.

On the other hand, in Figure 6 we show the photon indices Γ_1 and Γ_2 versus kT_e of the Comptb1 (red points) and Comptb2 (blue points) components (see also Table 4). The decreasing index phase of the Comptonization component is strongly related to the high electron temperature ($kT_e^{(2)} > 85$ keV). That index remains constant when the electron temperature $kT_e^{(2)}$ varies within the range 3–85 keV.

Our Comptonization model demonstrates a high quality for all data sets. The value of $\chi_{red}^2 = \chi^2/N_{dof}$, where N_{dof} is a number of degree of freedom, is about 1.0. Only for less than 2% of the spectra does χ_{red}^2 reach 1.4. But χ_{red}^2 never exceeds a rejection limit of 1.5 which corresponds to a 90% confidence level.

3.3.1. Light curve and related spectral characteristics

A complex behavior in a wide range of timescales, from seconds to years, is seen in the X-ray light curve of 4U 1705–44 (e.g., BO02). In this section we present the source variability from hours to days. In Figure 10 we show the source and model parameter evolution for the

whole set of the observed spectra. Here, from the top to the bottom, we present the evolution of the count rate (in counts s^{-1}) in the 2–9 keV range using the 16 s time resolution; of the hardness ratio HC $[10\text{--}50\text{ keV}]/[3\text{--}10\text{ keV}]$; the model flux in the 3–10 keV and 10–50 keV energy ranges (black and green points, respectively); $kT_e^{(1)}$ (red) and $kT_e^{(2)}$ (blue), the normalizations N_{Com1} (red) and N_{Com2} (blue) and $\alpha = \Gamma - 1$ for *Comptb1* (red points) and *Comptb2* (blue points) for *R1 – R3* sets corresponding to the time period from MJD 50,380 to MJD 51,650.

The light-curve intervals, corresponding to values of $\Gamma_2 < 2$ are shown by blue vertical strips. For these phases the electron temperatures $kT_e^{(2)}$ is extremely high, while the ratio $[10\text{--}50\text{ keV}]/[3\text{--}10\text{ keV}]$ coefficient (HC) is arbitrary. It should be also noted that a hardness ratio is very sensitive to the choice of energy bands, as shown above (see Fig. 3).

All *hard* \rightarrow *soft* transitions of 4U 1705-44 (see third panel from the top) are related to a significant increase of the 3–10 keV flux and thus to a decrease of the HC coefficient. Furthermore, one can also see from Figure 10 how the electron temperature $kT_e^{(2)}$ (blue points) drops from 95 keV to 5 keV during the hard-to-soft transitions (island-banana cycle). $kT_e^{(2)}$ reaches its maximum at the UB branch (e.g. at MJD 51,301). In Fig. 7 we present the corresponding X-ray spectrum for this branch. Note that $kT_e^{(1)}$ (red points) varies from 3 to 20 keV, indicating that the Comptonization component related to the innermost region of the transition layer, next to the NS surface, is much cooler than the TL outer part related to $kT_e^{(2)}$.

The normalizations N_{Com1} (red points) and N_{Com2} (blue points) are only weakly correlated with a coefficient HC (hardness ratio color) and count rate in the 2-9 keV band. In fact, for all spectral states the NS emission always dominates (see Figure 10). N_{Com2} is variable (see Table 4). Furthermore, N_{Com2} (or \dot{M}) correlates with an increase of $T_e^{(2)}$ during X-ray flares (see panels 2-4 from the bottom of Fig. 10).

The fractional contribution of the Comptonized component associated with the seed disk photons (related to N_{Com2}) is always much weaker than that contributed by the NS seed photons (related to N_{Com1}). In fact, $N_{Com2} \sim 0.1N_{Com1}$. As we show in the bottom panel of Figure 10, α_1 and α_2 ($\Gamma_{1,2} = \alpha_{1,2} + 1$) only slightly vary with time around 1, except for five points where α_2 drops from this level.

The seed photon temperatures kT_{s1} and kT_{s2} increase from 1.3 to 1.5 keV (for the *Comptb1*) and from 1.1 to 1.3 keV (for the *Comptb2*), respectively, during banana (soft state) \rightarrow island (hard state) transition. In order to evaluate the changes of a size of the seed photon region during the state transtion, we use the parameters obtained by the Comptb models (see Tables 3 and 4).

Furthermore, to evaluate the radius of the illuminated TL region by the seed photons that are finally Comptonized, we assume that the seed photon emission is a BB and the total Comptonized flux is $F_{Com} = \eta F_{seed}$ where η is an enhancement Comptonization factor (which is $(4/5)[\log(T_e/T_s)+1.5]$ for the case $\alpha = 1$ ($\Gamma = \alpha+1 = 2$), see Sunyaev & Titarchuk (1980)). But F_{seed} is obtained as

$$F_{seed} = \sigma T_{s,ef}^4 (R_{seed}/D)^2, \quad (2)$$

and so an apparent radius of the seed photon area is defined by

$$R_{seed} = 3 \times 10^4 D \frac{\sqrt{F_{com}/\eta}}{T_{s,ef}^2} \text{ km}, \quad (3)$$

where D is the distance in kpc, $T_{s,ef} \sim T_{s1}$ is in keV, $F_{seed} = F_{Com}/\eta$, F_{Com} is the Comptonized radiation and F_{seed} and F_{Com} are in $\text{erg cm}^{-2} \text{ s}^{-1}$. By considering the F_{Com} obtained using the *RXTE* spectra we find that $F_{Com} \sim 9.64 \times 10^{-9}$ and $9.5 \times 10^{-10} \text{ erg cm}^{-2} \text{ s}^{-1}$ in the BS and IS, respectively. We use a distance D of 7.4 kpc, to obtain $R_{seed} \sim 5.6 \text{ km}$ in the BS and $R_{seed} \sim 1.6 \text{ km}$ in the IS state, respectively. We should emphasize that the above estimates of R_{seed} are related to the effective area of the seed photons which is $4\pi R_{seed}^2$ is in our case. This area is definitely less than the NS area $4\pi R_{NS}^2$ as it should be.

As for the BB component, in the BS and IS, the BB temperature, T_{BB} is about 0.6 keV. In turn, the BB radius R_{BB} is derived via $L_{BB} = 4\pi R_{BB}^2 \sigma T_{BB}^4$, where L_{BB} is the BB luminosity and σ is the Stefan–Boltzmann constant. Assuming a distance D of 7.4 kpc [see Haberl & Titarchuk (1995)] the BB region has an apparent radius R_{BB} , which varies from 5.5 km (in the IS) to 120 km (in the BS). These values are in agreement with the emission coming from the AD (see Fig. 4). Thus, the radii R_{seed} and R_{BB} have reasonable values that are compatible with the adopted model (see Sect. 3.2.1).

4. Discussion

4.1. Comparative analysis of spectral properties of Z- and Atoll sources

In this section we investigate how the X-ray spectral characteristics depend on \dot{M} variation relying on X-ray observations of 4U 1705-44 during its spectral evolution across the banana-island branches. In fact, we discover a new type of Γ –index behavior in 4U 1705-44 with respect to other known accreting NS sources. But variation of the index in 4U 1705-44 is quite similar to that observed in the prototypical Z-source Sco X-1. Thus, it is worth comparing 4U 1705-44 with other NS binaries and identifying differences and similarities of

these sources (see Table 5). We make a comparison with six sources: *Z*-sources GX 340+0 (STF13), Sco X-1 (STS14), and *atolls* 4U 1705-44, 4U 1728-34 (ST11), GX 3+1 (ST12) and 4U 1820-30 (TSF13), using the same double *Comptb* spectral model. We also confront the spectral evolution of 4U 1705-44 with that in XTE J1701-462 (NS source) since these two objects demonstrate spectral properties common to *Z*-sources and *atolls* depending on their X-ray luminosity.

4.1.1. Approximate Constancy of the Photon index versus the Electron Temperature

Z-sources GX 340+0 and Sco X-1, and *atolls*, 4U 1728-34, 4U 1820-30, GX 3+1, show a quite similar behavior of Γ versus T_e at relatively low electron temperatures ($3 \text{ keV} < kT_e < 60 \text{ keV}$). The spectral index Γ_2 is almost constant at a value of approximately about 2. This index behavior can presumably indicate that, for these five sources, the accreted material releases its gravitational energy in the whole transition layer (TL) (see ST11, FT11, ST12, STF13, TSF13, and TSS14). According to the TSS14 model, this energy release is much higher in the TL than the cooling flow of the soft disk photons.

For Sco X-1 (TSS14) and 4U 1705-44 we find a wider range of T_e than that in other *atolls* and *Z*-sources. Moreover, Sco X-1 gives us a possibility to identify the index sample when $L > L_{\text{Edd}}$. It is worth noting that in this case the resulting luminosity is less than or equal to the critical one, whose value depends on the plasma (electron) temperature value. We find that Γ_2 substantially decreases when $kT_e > 85 \text{ keV}$ (for 4U 1705-44 at UB) and $kT_e > 60 \text{ keV}$ (for Sco X-1 at FB) (see Fig. 11). In 4U 1705-44 the photon index of the hard tail Γ_2 changes between 1.4 and 2 in upper banana state. A similar case behavior also takes place in Sco X-1 at FB (see TSS14), where the photon index Γ_2 varies between 1.3 and 2. when the electron temperature of the TL is high ($60 \text{ keV} < kT_e < 200 \text{ keV}$).

Note that only two sources, 4U 1705-44 and Sco X-1 demonstrate a decrease of Γ_2 at high kT_e . The decreasing index phase of 4U 1705-44 begins at a higher electron temperature ($kT_e \sim 80 \text{ keV}$) than that in Sco X-1 ($kT_e \sim 60 \text{ keV}$). On the other hand, the upper limit of T_e ranging is higher in Sco X-1 (kT_e^{max} exceeds 100 keV) than that for 4U 1705-44 ($kT_e^{\text{max}} \sim 95 \text{ keV}$), which is possibly related to different X-ray luminosity levels (for *atolls* and *Z*-sources). However, 4U 1705-44 emits very close to a *Z*-source luminosity range as can be seen from Fig. 8.

We contrast our results for *Z*-sources and *atolls* with the spectral behavior of XTE J1701-462 (see Lin et al. 2009, hereafter LRH09). This source evolves from the *atoll* to *Z*-stage and finally reaches the Eddington luminosity. It is surprising that during the hard spectral

state of XTE J1701-462 the photon index obtained by LHR09 is close to 2, while in the soft state the index Γ increases up to 2.5. Note, that LHR09 investigate the spectrum in the 3–80 keV energy range only. It is possible that XTE J1701-462 is a unique NS object, which somehow differs from the standard atoll and Z-sources. In fact, LHR09 use various models to fit the data, and their models take into account the role of a weak Comptonization in the soft state and in the hard state.

5. CONCLUSIONS

We have investigated the spectral property correlations with mass accretion rate found in 4U 1705-44 using *BeppoSAX* and *RXTE*. We establish that the broadband energy spectra during all atolls can be described by the double Comptb additive model. These two Comptonized components are related to the different seed photon temperatures ($T_{s1} \sim 1.5$ keV and $T_{s2} = 1.1 - 1.3$ keV). To improve the fit quality we also include an iron-line (Gaussian) component.

Spectral modeling 4U 1705-44 gives us a possibility to separate two distinct zones of the spectral formation along the atoll track. One is associated with the hard component while the other is related to the soft component. We find that the hard-to-soft spectral transition is driven by mass accretion rate \dot{M} . In fact, N_{Com1} and N_{Com2} (normalization parameters; see Eq. 1) of the Comptonized components are linearly related to mass accretion rate, \dot{M} . We establish an increase of N_{Com2} (or \dot{M}), which correlates with an increase of the electron temperature $kT_e^{(2)}$ during X-ray flares (see second and third panels from the bottom of Fig. 10).

We establish the stability of both photon indices Γ_1 and Γ_2 around 2 during the ISs and BSs, which correspond to the range of the CC (TL) electron temperature of $kT_e^{(2)}$ from 3 keV to 85 keV, while the decrease of Γ_2 is observed during the high electron temperature phase ($kT_e^{(2)} > 85$ keV). We explain the observed stability of $\Gamma_{1,2}$ within 2 using a model in which the energy deposition takes place in the TL and the energy release dominates the disk photon flux. This result is similar to what was previously found in the atolls 4U 1728-34, 4U 1820-30 and GX 3+1 and Z-source GX 340+0 through all spectral states and in Z-source Sco X-1 during HB–NB–botFB. In addition to this index plateau phase, of $\Gamma_{1,2} \sim 2$ we also find the decreasing index Γ_2 *detected* over the UB (like that established in Sco X-1 at FB). We interpret this index decrease using the TSS14 model, where the energy release occurs only in some outer part of the TL. In fact, the radiation pressure halts the accretion flow in the innermost part of the TL, where the plasma temperature is effectively dictated by the NS surface photons. Thus, the electron (Klien-Nishina) cross-section increases with

diminishing T_e (see §4 of TSS14 for details).

During this decreasing index stage, the spectra of 4U 1705-44 and Sco X-1 exhibit an increase of T_e of the *hard* Comptonization tail. Note that in BHs the index rises and then saturates when \dot{M} increases. These indices behave in a manner drastically different from that seen in the NS sources, Sco X-1 and 4U 1705.

We suggest that the robust nature of the parameter interdependencies resulting from the application of our model points to fundamental insights into the complex, and poorly understood, behavior of LMXBs.

Acknowledgments: We recognize a contribution of the referee who has thoroughly checked the paper context. N. Shaposhnikov also acknowledges the support of this research by the NASA under Grant NNX13AF39G.

REFERENCES

- Barret, D., Olive, J.-F. 2002, ApJ, 578, 391 (BO02)
- Boella G., Butler R. C., Perola G. C., et al., 1997, A&A, 122, 299
- Bradshaw, C.F., Fomalont, E.B. & Geldzahler, B. J, 1999, ApJ, 512, L121
- Church, M. J., Gibiec, A. & Bałucińska-Church, M. 2014 MNRAS, 438, 2784
- Christian, D.J. & Swank, J. H. 1997, ApJS, 109, 177
- D’Ai, A. et al. 2012, A&A 543, A20
- D’Ai, A., Di Salvo, T., Ballantyne, D., et al. 2010, A&A, 516, id.A36
- D’Ai, A., Zycki, P., Di Salvo, T., Iaria, R., Lavagetto, G. & Robba, N. R. 2007, ApJ, 667, 411
- D’Amico, F., Heindl, W. A., Rothschild, R. E. et al. 2001, ApJ, 547, L147
- Di Salvo, T., Iaria, R., A., Iaria, R. et al. 2015, MNRAS, 449, 2794
- Di Salvo, T., D’Ai, A., Iaria, R. et al. 2009, MNRAS, 398, 2022
- Di Salvo, T., Goldoni, P., Stella, L. et al. 2006, ApJ, 649, L91
- Di Salvo, T., Iaria, R., Mendez, M., et al. 2005, ApJ, 623, L121

- Di Salvo, T., Mendez, M. & van der Klis, M. 2003, A&A, 406, 177
- Di Salvo, T., Mendez, M., van der Klis, M., Ford, E. & Robba, N.R. 2001 ApJ, 546, 1107
- Di Salvo, T., Stella, L., Robba, N. R. et al. 2000, ApJ, 544, L119
- Egron, E., Di Salvo, T., Motta, et al. 2013, A&A, 550, 5
- Farinelli, R., Paizis, A., Landi, R., & Titarchuk, L. 2009, A&A, 498, 509
- Fender, R. P., & Hendry, M. A., 2000, MNRAS, 317, 1
- Fiocchi, M., Bazzano, A. & Ubertini, P. et al. 2007, ApJ, 657, 448
- Ford, E.C. et al. 2000, ApJ, 537, 368
- Ford, E. C., van der Klis, M., & Kaaret, P. 1998, ApJ, 498, L41
- Frontera, F., Costa, E., dal Fiume, D. et al. 1997, A&AS, 122, 357
- Gierlinski, M. & Done, C. 2002, MNRAS, 331, L47
- Haberl F. & Titarchuk L. 1995, A&A, 299, 414
- Hasinger, G., & van der Klis, M. 1989, A&A, 225, 79
- Hjellming, R. M., Stewart, R. T., White, G. L. 1990, ApJ, 365, 681
- Homan, J., van der Klis, M., Fridriksson, J. K., 2010, ApJ, 719, 201
- Jonker, P. G., Wijnands, R., van der Klis, M. et al. 1998, ApJ, 499, L191
- Kuulkers, E & van der Klis, M. 2000, A&A, 356, L45
- Langmeier, A. A, Sztajno, M., Hasinger, G. et al. 1987, ApJ, 323, 902
- Levine, A. M., Bradt, H., Cui, W., et al. 1996, ApJ, 469, L33
- Lin, D., Remillard, R.A. & Homan, J. 2009, ApJ, 696, 1257 (LRH09)
- Lin, D., Homan, J., Remillard, R., & Wijnands, R. 2007, Astron. Tel., 1183
- Manzo G., Giarrusso S., Santangelo A., et al. 1997, A&AS 122, 341
- Muno, M.P., Remillard, R. A. & Chakrabarty, D. 2002, ApJ, 568, L35
- Piraino, S., Santangelo, A., Di Salvo, T., et al. 2007, A&A 471, L17

- Paizis, A., Farinelli, R., Titarchuk, L. et al. 2006, *A&A*, 459, 187
- Parmar, A., Martin, D. D. E., Bavdaz, M. et al. 1997, *A&AS*, 122, 309
- Sanna, A., Méndez, M., Altamirano, D., Homan, J., et al. 2010, *MNRAS*, 408, 622
- Sztajno M., Langmeier, A., Frank, J. et al. 1985, *IAU Circ No.* 4111
- Seifina, E., Titarchuk, L., & Shaposhnikov, N. 2013, *ApJ*, 789, 57 (STS14)
- Seifina, E., Titarchuk, L., & Frontera, F. 2013, *ApJ*, 766, 63 (STF13)
- Seifina, E. & Titarchuk, L. 2012, *ApJ*, 747, 99 (ST12)
- Seifina, E. & Titarchuk, L. 2011, *ApJ*, 738, 128 (ST11)
- Shakura, N.I., & Sunyaev, R.A. 1973, *A&A*, 24, 337
- Shaposhnikov, N. & Titarchuk L. 2004, *ApJ*, 606, L57
- Smale, A. P., Zhang, W., & White, N. E. 1997, *ApJL*, 483, L119
- Strohmayer, T. 1998, *AIP Conference Proceedings*, Volume 431, pp. 397-400 in *American Institute of Physics Conference Series*, (astro-ph/9802022v1)
- Sunyaev, R.A. & Titarchuk, L. 1980, *A&A*, 86, 121
- Titarchuk, L., Seifina, E. & Shrader, Ch. 2014, *ApJ*, 798, 98 (TSS14)
- Titarchuk, L., Seifina, E., & Frontera, F. 2013, *ApJ*, 767, 160 (TSF13)
- Titarchuk, L.G. & Osherovich, V.A. 1999, *ApJ*, 518, L95
- Titarchuk, L., Lapidus, I.I. & Muslimov, A. 1998, *ApJ*, 419, 315
- van Paradijs, J. 1978, *Nature*, 274, 650
- van Straaten, S., Ford, E., van der Klis, M., Méndez, M. & Kaaret, Ph. 2000, *ApJ*, 540, 1049
- Zhang, C.M. et al. 2006, *MNRAS*, 366, 1373

Table 1. The list of *BeppoSAX* observations of 4U 1705-44 used in our analysis.

Number of Set	Obs. ID	Start Time (UT)	End Time (UT)	MJD Interval
S1	21292001	2000 Aug 20 16:20:16	2000 Aug 21 19:22:57	51776.6-51777.8
S2	21292002	2000 Oct. 3 12:30:07	2000 Oct. 4 21:11:38	51820.5-51821.9
References. (1) Fiocchi et al. (2007); (2) Piraino et al. (2007); (3) Egron et al. (2013).				

Table 2. The list of groups of *RXTE* observation of 4U 1705-44

Number of Set	Dates, MJD	<i>RXTE</i> Proposal ID	Dates UT
R1	50,539-50,542	20073 (1)	1997 Apr. 1–4 1997
	50,495-50,748	20074 (1), (2)	1997 Feb. 16–Oct. 27
	50,398-50,587	20161 (1)	1996 Nov. 11–1997 May 19, 1997
R2	51,290-51,583	40034 (1), (3)	1999 Apr. 22–2000 Feb. 2
R3	51,219-51,247	40051 (1), (2)	1999 Feb. 10– Mar. 10
References: (1) Muno et al. (2002); (2) Barret & Olive (2002); (3) Egron et al. (2013).			

Table 3. Best-fit Parameters of Comparative Spectral Analysis of *BeppoSAX* and *RXTE* Observations of 4U 1705-44 in the 0.3–200 keV Energy Range Using Two Additive models[†]: wabs*(Blackbody + Comptb + powerlaw + Gaussian) and wabs*(Blackbody + Comptb1 + Comptb2 + Gaussian).

Source state		IS	IS	LB	LB	UB
Satellite		<i>BeppoSAX</i>	<i>RXTE</i>	<i>BeppoSAX</i>	<i>RXTE</i>	<i>RXTE</i>
Model	Parameter	21292002	40034-01-07-02G	21292001	40034-01-02-09	40034-01-02-06
wabs	N_H ($\times 10^{22}$ cm $^{-2}$)	2.36 \pm 0.07	4.6 \pm 0.1	1.81 \pm 0.02	4.65 \pm 0.02	4.82 \pm 0.07
bbody	kT $_{BB}$ (keV)	0.50 \pm 0.03	0.5 \pm 0.1	0.62 \pm 0.03	0.61 \pm 0.03	0.59 \pm 0.01
	$N_{BB}^{\dagger\dagger}$	3.8 \pm 0.3	7.8 \pm 0.3	2.7 \pm 0.4	100.7 \pm 0.9	14.9 \pm 0.2
Comptb	$\alpha = \Gamma - 1$	1.00 \pm 0.01	1.06 \pm 0.04	0.99 \pm 0.03	1.02 \pm 0.04	1.05 \pm 0.06
	kT $_s$ (keV)	1.31 \pm 0.08	1.30 \pm 0.02	1.36 \pm 0.06	1.28 \pm 0.09	1.30 \pm 0.07
	log(A)	0.92 \pm 0.06	0.95 \pm 0.02	-0.03 \pm 0.01	-0.24 \pm 0.09	-0.22 \pm 0.02
	kT $_e$ (keV)	20.66 \pm 0.08	21.51 \pm 0.09	2.78 \pm 0.08	2.86 \pm 0.09	2.78 \pm 0.03
	$N_{Com}^{\dagger\dagger}$	1.08 \pm 0.03	0.13 \pm 0.02	5.56 \pm 0.02	6.62 \pm 0.01	7.16 \pm 0.07
Power law	Γ_{pow}	1.88 \pm 0.05	1.5 \pm 0.4	2.54 \pm 0.05	3.97 \pm 0.05	1.90 \pm 0.07
	$N_{pow}^{\dagger\dagger}$	2.95 \pm 0.02	2.13 \pm 0.01	1.26 \pm 0.02	1.42 \pm 0.01	1.16 \pm 0.07
Gaussian	E $_{line}$ (keV)	6.45 \pm 0.08	6.48 \pm 0.09	6.80 \pm 0.07	6.81 \pm 0.05	6.90 \pm 0.07
	σ_{line} (keV)	0.35 \pm 0.04	0.40 \pm 0.06	0.39 \pm 0.07	0.41 \pm 0.03	0.41 \pm 0.05
	$N_{line}^{\dagger\dagger}$	1.08 \pm 0.03	1.13 \pm 0.02	0.76 \pm 0.02	0.72 \pm 0.01	0.66 \pm 0.07
χ^2_{red} (dof)		3.28 (193)	1.78 (79)	2.3 (200)	1.34 (77)	1.16 (77)
wabs	N_H ($\times 10^{22}$ cm $^{-2}$)	2.16 \pm 0.04	2.3 \pm 0.1	2.43 \pm 0.03	4.3 \pm 0.1	4.4 \pm 0.1
bbody	kT $_{BB}$ (keV)	0.54 \pm 0.07	0.60 \pm 0.04	0.56 \pm 0.03	0.60 \pm 0.05	0.60 \pm 0.04
	$N_{BB}^{\dagger\dagger}$	0.43 \pm 0.01	0.15 \pm 0.03	4.49 \pm 0.05	3.12 \pm 0.02	3.16 \pm 0.05
Comptb1	$\alpha_1 = \Gamma_1 - 1$	1.00 \pm 0.04	0.98 \pm 0.02	0.99 \pm 0.07	1.01 \pm 0.02	1.00 \pm 0.03
	kT $_{s1}$ (keV)	1.42 \pm 0.03	1.5 \pm 0.1	1.75 \pm 0.02	1.50 \pm 0.03	1.50 \pm 0.04
	log(A_1)	0.93 \pm 0.06	2.0 †††	-0.04 \pm 0.01	-4.02 \pm 0.07	0.4 \pm 0.2
	kT $_e^{(1)}$ (keV)	18.9 \pm 0.02	9.22 \pm 0.09	2.47 \pm 0.04	2.71 \pm 0.09	20.4 \pm 0.3
	$N_{Com1}^{\dagger\dagger}$	1.08 \pm 0.02	0.04 \pm 0.02	5.28 \pm 0.06	5.54 \pm 0.08	4.58 \pm 0.04
Comptb2	$\alpha_2 = \Gamma_2 - 1$	1.01 \pm 0.03	1.01 \pm 0.02	1.00 \pm 0.03	1.01 \pm 0.01	0.41 \pm 0.07
	kT $_{s2}$ (keV)	1.32 \pm 0.1	1.27 \pm 0.03	1.29 \pm 0.05	1.26 \pm 0.02	1.09 \pm 0.03
	log(A_2)	-0.03 \pm 0.01	0.5 \pm 0.2	-1.04 \pm 0.02	-0.22 \pm 0.02	-0.25 \pm 0.03
	kT $_e^{(2)}$ (keV)	51 \pm 1	83 \pm 5	2.04 \pm 0.08	64 \pm 5	96 \pm 7
	$N_{Com2}^{\dagger\dagger}$	0.20 \pm 0.07	0.11 \pm 0.08	0.24 \pm 0.05	10.12 \pm 0.06	0.48 \pm 0.01
Gaussian	E $_{line}$ (keV)	6.51 \pm 0.08	6.40 \pm 0.05	6.95 \pm 0.04	6.57 \pm 0.03	6.67 \pm 0.03
	σ_{line} (keV)	0.60 \pm 0.04	0.56 \pm 0.07	0.79 \pm 0.08	0.64 \pm 0.07	0.69 \pm 0.07
	$N_{line}^{\dagger\dagger}$	1.07 \pm 0.09	1.09 \pm 0.08	0.68 \pm 0.09	0.95 \pm 0.02	1.15 \pm 0.04
χ^2_{red} (dof)		1.02 (296)	0.76 (86)	1.07 (295)	1.02 (86)	1.05 (86)

[†] Errors are given at the 90% confidence level. ^{††} The normalization parameters of blackbody and Comptb components are in units of L_{37}^{soft}/d_{10}^2 erg/s/kpc 2 , where L_{37}^{soft} is the soft photon luminosity in units of 10^{37} erg s $^{-1}$, d_{10} is the distance to the source in units of 10 kpc, the Gaussian component is in units of $10^{-3} \times total \text{ photons cm}^{-2} \text{ s}^{-1}$ in line, *powerlaw* component is in units of $10^{-2} \times photons \text{ keV}^{-1} \text{ cm}^{-2} \text{ s}^{-1}$ at 1 keV; ^{†††} when parameter $\log(A) \gg 1$, it is fixed to a value 2.0 for the model **Comptb** (see comments in the text).

Table 4. Best-fit Parameters of Spectral Analysis of PCA+HEXTE/*RXTE* Observations of 4U 1705-44 in the 3 – 200 keV Energy Range[†]. Parameter errors are given at the 90% confidence level.

Observational ID	MJD, (day)	$\alpha_1 =$ $\Gamma_1 - 1$	$kT_e^{(1)}$, (keV)	$\log(A_1)$	$N_{Com1}^{\dagger\dagger\dagger}$	$N_{Bbody}^{\dagger\dagger\dagger}$	$kT_{s2}^{\dagger\dagger\dagger}$, (keV)	$\alpha_2 =$ $\Gamma_2 - 1$	$kT_e^{(2)}$, (keV)	$\log(A_2)$	$N_{Com2}^{\dagger\dagger\dagger}$	E_{line} , (keV)	$N_{line}^{\dagger\dagger\dagger}$	χ_{red}^2 (dof)
20073-04-01-00	50539.56	0.99(1)	7.72(8)	2.00 ^{††}	0.91(6)	0.49(7)	1.31(3)	1.04(3)	20(1)	1.7(1)	0.59(4)	6.97(4)	0.28(8)	1.45(87)
20073-04-01-01	50571.69	1.00(2)	2.48(9)	2.00 ^{††}	1.92(3)	1.5(1)	1.26(2)	1.01(2)	33(2)	1.77(4)	0.58(3)	6.96(2)	0.24(9)	0.91(87)
20073-04-01-02	50542.32	1.03(1)	2.5(1)	2.00 ^{††}	1.51(2)	1.5(1)	1.23(4)	1.00(6)	40(1)	-0.66(2)	0.42(4)	6.97(3)	0.25(4)	0.79(87)
20073-04-01-03	50542.49	1.01(1)	2.44(9)	2.00 ^{††}	1.86(1)	1.6(2)	1.28(2)	0.99(1)	45(3)	0.43(5)	7.4(1)	6.94(4)	0.29(1)	0.83(87)
20074-02-01-00	50495.75	1.02(4)	2.38(7)	2.00 ^{††}	1.93(5)	1.8(1)	1.19(3)	0.97(3)	50(1)	2.00 ^{††}	0.01(1)	6.95(7)	0.31(2)	0.87(86)
20074-02-02-00	50536.55	0.97(1)	16.9(2)	2.00 ^{††}	0.08(2)	3(1)	1.29(4)	0.98(2)	57(2)	2.00 ^{††}	0.09(2)	6.95(4)	5.1(9)	0.75(88)
20074-02-03-00	50608.80	0.96(6)	2.52(4)	0.28(3)	11.9(2)	3.0(1)	1.25(2)	1.00(1)	69(5)	-0.63(2)	8.4(7)	6.97(3)	8(1)	0.92(88)
20074-02-04-00	50650.48	1.01(1)	2.51(4)	0.24(2)	11.9(4)	3.05(2)	1.26(6)	1.01(1)	60(2)	-0.64(3)	7.9(1)	6.95(4)	8.2(3)	0.91(88)
20074-02-05-00	50693.16	0.99(1)	2.54(3)	0.14(5)	8.6(3)	1.11(9)	1.29(2)	0.99(2)	51(3)	-0.61(4)	0.39(1)	6.74(5)	6.4(2)	0.81(88)
20074-02-06-00	50721.58	0.98(4)	2.53(5)	0.11(6)	9.1(2)	3.44(8)	1.17(3)	0.98(4)	46(4)	-0.13(2)	0.13(3)	6.65(3)	7(1)	0.66(88)
20074-02-07-00	50748.19	1.01(1)	2.59(6)	0.07(4)	6.9(5)	4.90(7)	1.31(4)	1.01(2)	30(1)	2.00 ^{††}	0.1(1)	6.55(4)	6.2(4)	0.76(88)
20161-01-01-002	50398.35	0.99(3)	3.12(6)	-2.3(8)	0.20(1)	0.39(6)	1.28(2)	0.99(1)	50(2)	0.43(2)	0.34(2)	6.40(4)	2.1(3)	1.50(89)
20161-01-01-01	50396.35	1.03(4)	12.2(4)	-1.9(6)	8(1)	0.25(4)	1.26(3)	1.02(4)	30(1)	4.43(2)	0.13(1)	6.41(3)	1.2(1)	0.96(92)
20161-01-01-03	50398.95	0.99(1)	7.4(2)	-1.8(5)	0.09(2)	0.26(5)	1.27(4)	1.01(2)	22.8(3)	1.25(6)	0.30(2)	6.42(2)	2.6(2)	1.27(89)
20161-01-02-00	50584.46	1.03(3)	8.0(1)	2.00 ^{††}	0.20(1)	0.301(5)	1.12(2)	0.83(6)	90(2)	0.66(6)	0.86(1)	6.40(5)	1.9(1)	1.17(86)
20161-01-02-01	50585.46	1.00(1)	8.1(2)	-1.9(8)	0.10(3)	0.41(2)	1.27(3)	0.98(5)	95(8)	0.29(1)	0.59(3)	6.41(9)	2.8(3)	1.26(90)
20161-01-02-02	50586.47	1.00(4)	8.2(2)	-1.8(6)	0.12(3)	0.41(2)	1.28(4)	0.97(4)	39(2)	1.29(1)	0.58(1)	6.41(2)	3.6(2)	1.26(90)
20161-01-02-03	50587.35	0.97(2)	3.2(1)	-2.1(7)	0.08(1)	0.37(1)	1.31(3)	1.00(1)	31(2)	2.00 ^{††}	0.63(2)	6.39(5)	2.9(2)	1.25(89)
20161-01-02-04	50587.55	1.00(1)	3.7(2)	-1.8(5)	0.07(2)	0.38(3)	1.26(4)	0.98(6)	37(2)	2.00 ^{††}	0.67(5)	6.43(3)	1.5(1)	0.84(89)
40034-01-01-00	50584.46	0.99(2)	2.9(3)	-0.26(3)	7.12(7)	4.49(9)	1.29(2)	1.01(2)	61(4)	-0.16(1)	0.10(2)	6.45(7)	1.7(2)	0.85(87)
40034-01-01-01	51294.33	1.00(2)	2.50(6)	0.45(1)	7.10(8)	4.43(7)	1.19(3)	0.98(1)	43(1)	-0.15(1)	0.10(1)	6.76(5)	0.11(1)	1.15(86)
40034-01-01-02	51295.59	0.97(1)	3.10(1)	-0.17(1)	5.19(1)	4.49(9)	1.27(4)	1.00(1)	67(2)	-2.0(1)	0.20(5)	6.52(5)	0.35(1)	1.23(85)
40034-01-01-03	51297.53	1.00(5)	2.14(2)	-0.18(2)	5.40(2)	4.44(5)	1.25(2)	1.00(2)	63(2)	-1.95(3)	0.10(1)	6.61(5)	0.54(3)	1.12(85)
40034-01-01-04	51297.47	1.02(6)	2.43(1)	-0.28(1)	5.13(2)	4.47(4)	1.28(1)	1.02(1)	68(4)	-0.16(2)	0.60(1)	6.40(4)	0.25(2)	1.18(86)
40034-01-02-00	51298.15	1.01(1)	3.04(3)	-0.25(3)	4.54(2)	4.48(5)	1.26(3)	0.99(2)	51(3)	-0.14(1)	0.65(3)	6.59(5)	0.14(1)	1.19(86)
40034-01-02-01	51298.69	0.96(6)	2.69(1)	-0.27(1)	5.86(2)	4.46(6)	1.29(3)	1.01(1)	63(2)	-0.18(2)	0.63(1)	6.60(3)	0.58(1)	1.02(86)
40034-01-02-02	51298.76	1.00(1)	3.04(1)	-0.27(1)	5.27(3)	4.43(5)	1.25(2)	0.98(2)	51(3)	-0.13(1)	0.67(1)	6.44(5)	0.19(1)	1.15(86)

Table 4—Continued

Observational ID	MJD, (day)	$\alpha_1 =$ $\Gamma_1 - 1$	$kT_e^{(1)}$, (keV)	$\log(A_1)$	$N_{Com1}^{\dagger\dagger\dagger}$	$N_{Bbody}^{\dagger\dagger\dagger}$	$kT_{s2}^{\dagger\dagger\dagger}$, (keV)	$\alpha_2 =$ $\Gamma_2 - 1$	$kT_e^{(2)}$, (keV)	$\log(A_2)$	$N_{Com2}^{\dagger\dagger\dagger}$	E_{line} , (keV)	$N_{line}^{\dagger\dagger\dagger}$	χ_{red}^2 (dof)
40034-01-02-03	51298.83	0.99(3)	2.72(2)	-0.26(3)	5.90(3)	4.45(3)	1.32(4)	1.03(3)	64(5)	-0.16(2)	0.62(1)	6.71(3)	0.53(3)	0.95(86)
40034-01-02-04	51298.89	1.02(2)	2.97(1)	-0.29(2)	5.41(3)	4.44(5)	1.29(1)	0.99(1)	56(7)	-0.15(2)	0.61(3)	6.48(5)	0.29(2)	1.11(86)
40034-01-02-05	51301.53	1.00(1)	2.18(4)	-0.28(1)	5.73(1)	4.45(2)	1.28(3)	0.98(2)	41(3)	-0.16(2)	0.65(1)	6.55(8)	0.34(2)	1.23(86)
40034-01-02-06	51301.69	1.00(3)	20.4(3)	0.4(2)	4.58(4)	3.16(5)	1.09(3)	0.41(7)	96(7)	-0.25(3)	0.48(1)	6.67(3)	1.15(4)	1.05(86)
40034-01-02-07	51301.69	1.00(1)	2.48(5)	0.23(6)	6.13(1)	3.04(6)	1.29(2)	1.00(1)	61(3)	-0.15(2)	0.42(3)	6.56(5)	1.19(5)	1.00(86)
40034-01-02-08	51301.75	1.01(2)	2.52(3)	0.17(5)	5.95(7)	3.05(5)	1.28(3)	1.02(2)	43(1)	-0.18(1)	0.41(1)	6.66(7)	1.14(3)	1.06(86)
40034-01-02-09	51301.83	1.01(2)	2.71(9)	-4.02(7)	5.54(8)	3.12(2)	1.26(2)	1.01(1)	64(5)	-0.22(2)	0.12(6)	6.57(3)	0.95(2)	1.02(86)
40034-01-03-00	51324.06	0.97(3)	2.38(3)	0.17(7)	2.24(7)	1.44(6)	1.28(4)	0.99(1)	42(7)	-0.26(2)	0.31(3)	6.66(5)	0.40(1)	1.00(86)
40034-01-03-01	51324.20	1.00(1)	2.41(7)	0.22(9)	2.03(6)	1.45(3)	1.29(1)	1.00(1)	65(4)	-0.22(1)	0.34(1)	6.40(5)	0.44(2)	0.95(86)
40034-01-03-02	51325.17	0.99(2)	2.34(5)	0.43(8)	1.88(5)	1.46(5)	1.27(3)	0.97(4)	59(3)	-0.21(2)	0.32(1)	6.40(7)	0.42(1)	0.97(86)
40034-01-04-00	51362.67	1.00(1)	22.6(3)	2.00 ^{††}	0.08(2)	0.45(2)	1.30(2)	1.01(1)	63(4)	0.26(8)	0.3041	6.45(3)	2.8(6)	1.14(86)
40034-01-04-01	51366.14	0.96(4)	20.0(9)	2.00 ^{††}	0.04(2)	0.04(2)	1.28(3)	0.99(2)	58(1)	-0.42(9)	0.32(1)	6.48(5)	1.3(4)	1.21(86)
40034-01-04-02	51367.14	1.00(1)	19.0(8)	2.00 ^{††}	0.01(1)	0.01(1)	1.29(5)	1.01(2)	45(2)	-0.43(9)	0.34(3)	6.40(5)	1.1(2)	1.22(86)
40034-01-04-03	51369.20	1.01(2)	21(1)	2.00 ^{††}	0.05(2)	0.02(1)	1.30(4)	1.00(1)	38(4)	-0.42(9)	0.37(2)	6.41(7)	1.2(1)	1.24(86)
40034-01-04-04	51370.20	1.02(1)	18.0(9)	2.00 ^{††}	0.02(1)	0.01(1)	1.27(3)	0.98(3)	62(4)	-0.4(1)	0.38(5)	6.49(3)	1.2(1)	1.23(86)
40034-01-04-05	51373.46	0.98(2)	8.0(5)	2.00 ^{††}	0.03(1)	0.01(1)	1.31(4)	1.00(2)	52(3)	-0.51(6)	0.62(2)	6.40(6)	1.3(2)	1.17(86)
40034-01-05-00	51333.24	1.01(3)	3.0(1)	-0.23(2)	2.51(7)	2.40(1)	1.27(3)	1.01(1)	48(1)	-0.14(6)	0.63(4)	6.53(5)	0.16(2)	1.14(86)
40034-01-05-01	51334.42	1.00(2)	3.2(1)	-0.22(1)	2.28(6)	2.58(1)	1.24(2)	0.99(2)	46(3)	-0.14(6)	0.61(5)	6.60(5)	0.15(1)	0.88(86)
40034-01-05-02	51335.23	0.97(1)	3.0(4)	-0.26(1)	1.89(2)	2.30(1)	1.29(3)	1.01(2)	51(7)	-0.14(6)	0.62(2)	6.61(5)	5.1(4)	0.76(86)
40034-01-05-03	51336.09	1.02(2)	2.51(6)	-0.08(2)	1.43(3)	0.58(1)	1.28(4)	1.00(1)	69(3)	-0.37(6)	0.85(3)	6.50(3)	4.9(7)	0.79(86)
40034-01-05-04	51337.46	1.00(1)	2.60(5)	-0.12(3)	1.43(1)	0.57(1)	1.26(2)	0.98(4)	68.0	-0.36(6)	0.83(1)	6.53(6)	3.8(4)	0.84(86)
40034-01-05-05	51390.13	1.01(4)	20.7(5)	2.00 ^{††}	2.00(8)	0.35(4)	1.27(3)	0.97(6)	34(6)	-2.1(9)	0.45(3)	6.40(5)	4.7(4)	1.07(86)
40034-01-05-06	51333.05	0.99(1)	2.67(6)	-0.17(3)	1.44(1)	0.58(1)	1.25(4)	1.00(1)	60(4)	-0.36(6)	0.65(1)	6.51(4)	2.1(3)	0.89(86)
40034-01-05-07	51392.27	1.02(2)	14.1(9)	2.00 ^{††}	2.00(8)	0.78(4)	1.11(2)	0.92(5)	92(3)	-1.10(9)	0.37(3)	6.56(3)	0.30(2)	1.13(86)
40034-01-06-00	51396.23	1.00(1)	2.91(5)	2.00 ^{††}	1.90(7)	0.58(1)	1.27(2)	0.98(4)	79(4)	-2.00(6)	3.17(1)	6.67(5)	4.3(4)	1.08(86)
40034-01-06-01	51436.15	0.99(1)	2.59(2)	2.00 ^{††}	5.42(8)	0.54(5)	1.29(3)	1.01(1)	81(2)	-2.1(2)	6.32(1)	6.95(7)	9.0(4)	1.08(86)
40034-01-06-09	51401.39	1.00(3)	2.76(4)	2.00 ^{††}	2.95(8)	0.56(3)	1.30(1)	1.02(2)	78(5)	-2.2(3)	3.99(8)	6.68(6)	5.2(4)	1.18(86)

Table 4—Continued

Observational ID	MJD, (day)	$\alpha_1 =$ $\Gamma_1 - 1$	$kT_e^{(1)}$, (keV)	$\log(A_1)$	$N_{Com1}^{\dagger\dagger\dagger}$	$N_{Bbody}^{\dagger\dagger\dagger}$	$kT_{s2}^{\dagger\dagger\dagger}$, (keV)	$\alpha_2 =$ $\Gamma_2 - 1$	$kT_e^{(2)}$, (keV)	$\log(A_2)$	$N_{Com2}^{\dagger\dagger\dagger}$	E_{line} , (keV)	$N_{line}^{\dagger\dagger\dagger}$	χ_{red}^2 (dof)
40034-01-07-00	51564.13	1.03(1)	20.7(7)	2.00 ^{††}	0.06(1)	0.18(1)	1.28(2)	0.99(1)	76(3)	0.2(1)	0.11(3)	6.43(5)	1.3(5)	1.06(86)
40034-01-07-01	51565.33	1.00(1)	20.7(5)	2.00 ^{††}	0.08(1)	0.16(1)	1.29(2)	1.02(2)	75(7)	0.2(1)	7(1)	6.41(3)	1.1(3)	1.07(86)
40034-01-07-02G	51566.26	0.98(2)	9.22(9)	2.00 ^{††}	0.04(2)	0.15(3)	1.27(3)	1.01(2)	83(5)	0.5(2)	0.11(8)	6.40(5)	1.0(1)	0.76(86)
40034-01-07-03	51573.72	0.99(3)	31.7(5)	2.00 ^{††}	0.04(1)	0.28(6)	1.26(4)	0.98(1)	70(7)	0.71(7)	0.26(9)	6.40(5)	1.2(2)	1.09(86)
40034-01-07-04	51569.32	1.00(1)	23.7(8)	2.00 ^{††}	0.12(7)	0.27(5)	1.28(2)	0.97(5)	41(4)	0.57(9)	0.33(8)	6.42(6)	1.3(1)	1.01(86)
40034-01-07-05	51574.65	0.97(4)	29.7(9)	2.00 ^{††}	0.16(6)	0.32(3)	1.27(3)	0.99(4)	73(3)	0.69(7)	0.44(9)	6.40(3)	1.4(2)	1.07(86)
40034-01-08-00	51572.65	1.00(2)	29(1)	2.00 ^{††}	0.07(6)	0.23(5)	1.29(2)	1.00(1)	52(7)	0.71(8)	0.20(9)	6.43(5)	1.1(1)	1.09(86)
40034-01-08-01	51575.90	1.00(1)	23.1(1)	2.00 ^{††}	0.23(5)	0.43(6)	1.27(4)	0.99(5)	49(3)	0.90(5)	0.63(9)	6.41(5)	1.8(5)	0.79(86)
40034-01-08-02	51577.03	0.99(2)	23.2(9)	2.00 ^{††}	0.24(6)	0.45(5)	1.26(3)	0.98(6)	44(2)	0.82(5)	0.65(7)	6.44(6)	3.2(1)	1.15(86)
40034-01-09-00	51581.76	1.04(1)	8.0(3)	2.00 ^{††}	0.11(1)	0.46(1)	1.11(2)	0.96(3)	25(4)	1.06(7)	1.01(2)	6.40(3)	6.1(3)	0.88(86)
40034-01-09-01	51580.84	1.00(1)	3.0(3)	2.00 ^{††}	0.21(4)	0.47(3)	1.30(3)	1.01(2)	21(5)	1.30(8)	0.89(1)	6.41(5)	3.2(2)	0.85(86)
40034-01-09-02	51578.78	0.99(2)	5.0(2)	2.00 ^{††}	0.52(2)	0.46(4)	1.29(4)	1.00(1)	20(3)	1.14(9)	0.76(1)	6.42(6)	3.1(1)	1.04(86)
40034-01-09-03	51583.10	1.00(3)	8.0(4)	2.00 ^{††}	0.10(1)	0.52(3)	1.27(1)	0.99(1)	24(2)	1.29(8)	0.99(3)	6.40(2)	6.3(3)	1.16(86)
40034-01-09-04	51580.04	1.02(1)	7.0(3)	2.00 ^{††}	0.20(3)	0.43(3)	1.29(1)	1.00(2)	32(7)	1.09(9)	0.84(7)	6.41(3)	4.7(2)	0.94(86)
40034-01-09-05	51581.68	0.99(3)	3.0(4)	2.00 ^{††}	0.10(1)	0.37(4)	1.31(2)	1.01(1)	29(3)	0.65(8)	1.27(2)	6.40(2)	0.13(1)	1.18(86)
40034-01-09-07	51581.69	1.00(1)	4.0(2)	2.00 ^{††}	0.45(1)	0.46(3)	1.30(1)	1.02(2)	26(4)	1.21(9)	0.96(1)	6.41(2)	5.4(2)	1.18(86)
40034-01-09-08	51583.17	0.96(4)	8.0(3)	2.00 ^{††}	0.54(2)	0.45(3)	1.29(3)	1.01(1)	28(2)	1.16(8)	1.02(1)	6.43(6)	4.3(3)	1.06(86)
40051-03-01-00	51219.60	1.00(1)	2.7(1)	0.11(1)	1.82(1)	1.92(1)	1.30(2)	1.00(1)	43(4)	-0.16(8)	0.19(2)	6.64(2)	0.11(1)	0.99(86)
40051-03-02-00	51221.60	1.01(2)	2.7(2)	2.00 ^{††}	1.56(2)	1.54(1)	1.29(4)	1.01(1)	35(2)	-0.13(8)	0.18(2)	6.51(6)	0.11(1)	1.12(86)
40051-03-03-00	51223.53	0.99(1)	4.11(9)	0.41(8)	0.65(8)	0.67(2)	1.08(2)	0.68(3)	95(3)	-0.14(8)	0.46(9)	6.40(3)	0.18(1)	1.17(86)
40051-03-04-00	51225.46	0.97(2)	6.2(1)	1.27(9)	0.40(6)	0.38(2)	1.29(2)	0.98(2)	37(1)	-0.17(8)	0.46(6)	6.41(2)	0.12(1)	1.03(86)
40051-03-05-00	51227.34	1.00(1)	29.9(4)	2.00 ^{††}	0.30(4)	0.34(2)	1.28(1)	1.00(1)	28(3)	-0.16(8)	0.19(5)	6.40(6)	4.8(2)	1.04(86)
40051-03-06-00	51229.59	1.02(4)	27.6(2)	2.00 ^{††}	0.27(1)	0.29(1)	1.30(4)	1.01(1)	34(5)	-0.12(8)	0.15(4)	6.45(2)	2.3(3)	0.95(86)
40051-03-07-00	51231.46	1.00(1)	30(2)	2.00 ^{††}	0.36(3)	0.33(1)	1.29(3)	1.00(2)	48(3)	-0.16(8)	0.24(3)	6.40(2)	5.6(4)	0.93(86)
40051-03-08-00	51233.27	0.99(3)	21(3)	2.00 ^{††}	0.36(2)	0.37(2)	1.27(2)	0.98(2)	87(2)	-0.09(4)	0.31(3)	6.47(3)	6.1(3)	1.06(86)
40051-03-09-00	51235.52	1.01(2)	26(2)	2.00 ^{††}	0.53(3)	0.41(5)	1.28(4)	1.00(1)	52(1)	2.00 ^{††}	0.35(5)	6.40(2)	6.2(3)	1.11(86)
40051-03-10-00	51237.52	1.00(1)	8.0(3)	2.00 ^{††}	0.60(5)	0.50(2)	1.29(2)	1.00(4)	35(3)	0.21(3)	0.46(4)	6.42(6)	9.5(4)	0.89(86)

Table 4—Continued

Observational ID	MJD, (day)	$\alpha_1 =$ $\Gamma_1 - 1$	$kT_e^{(1)}$, (keV)	$\log(A_1)$	$N_{Com1}^{\dagger\dagger\dagger}$	$N_{Bbody}^{\dagger\dagger\dagger}$	$kT_{s2}^{\dagger\dagger\dagger\dagger}$, (keV)	$\alpha_2 =$ $\Gamma_2 - 1$	$kT_e^{(2)}$, (keV)	$\log(A_2)$	$N_{Com2}^{\dagger\dagger\dagger}$	E_{line} , (keV)	$N_{line}^{\dagger\dagger\dagger}$	χ_{red}^2 (dof)
40051-03-11-00	51239.40	1.02(3)	6.70(4)	2.00 ^{††}	0.71(4)	0.53(3)	1.27(3)	1.02(2)	26(1)	0.34(3)	0.78(6)	6.48(2)	0.16(1)	0.97(86)
40051-03-12-00	51241.86	0.99(1)	8.1(2)	2.00 ^{††}	0.58(6)	0.58(2)	1.29(1)	1.01(1)	48(2)	0.54(6)	1.07(4)	6.40(3)	0.22(1)	1.02(86)
40051-03-13-00	51243.93	0.97(3)	5.0(3)	-0.67(3)	0.78(4)	0.83(2)	1.28(2)	0.98(4)	26(1)	0.96(4)	1.13(3)	6.59(2)	0.32(3)	1.07(86)
40051-03-14-00	51245.93	1.00(1)	3.10(7)	0.90(8)	1.13(2)	2.03(4)	1.30(1)	1.00(1)	2.32(7)	-0.20(3)	1.20(7)	6.61(2)	0.27(2)	1.11(86)
40051-03-15-00	51247.85	1.01(2)	3.60(9)	0.43(6)	1.17(3)	1.63(2)	1.29(3)	0.99(2)	3.49(8)	-0.45(5)	0.93(6)	6.58(5)	0.25(1)	1.06(86)

[†] The spectral model is $wabs * (blackbody + Comptb1 + Comptb2 + Gaussian)$; color temperature T_{BB} of the bbody component is fixed at 0.6 keV (see comments in the text); ^{††} parameter $\log(A_2)$ is fixed at 2.0 (see comments in the text), ^{†††} Normalization parameters of blackbody and Comptb components are in units of L_{37}/d_{10}^2 , where L_{37} is the source luminosity in units of 10^{37} erg/s, d_{10} is the distance to the source in units of 10 kpc and Gaussian component is in units of $10^{-2} \times total \text{ photons cm}^{-2} s^{-1}$ in line. ^{††††} kT_{s1} varies from 1.3 keV to 1.5 keV for the island to banana state transition while it is concentrated about 1.5 keV (see Fig. 9) for most of the spectra spectra, σ_{line} of Gaussian component is fixed to a value 0.7 keV (see comments in the text), N_H was free to vary within the range of $(2 - 4) \times 10^{22} \text{ cm}^{-2}$ (see comments in the text).

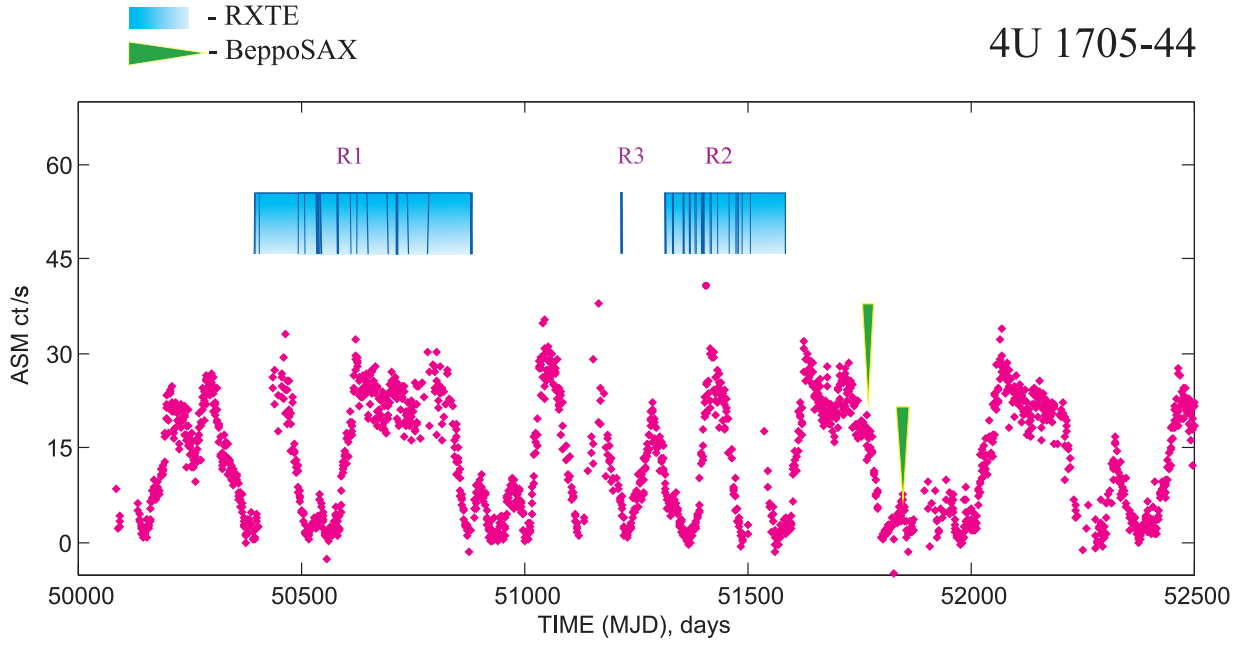


Fig. 1.— Evolution of ASM/*RXTE* count rate during 1997 – 2000 observations of 4U 1705-44. Green triangles show *BeppoSAX* NFI data, listed in Table 1, and blue vertical strips (on *top* of the panel) indicate a temporal distribution of the *RXTE* data of pointed observations used in our analysis, and bright blue rectangles indicate the *RXTE* data sets listed in Table 2.

Table 5. Comparisons of the Best-fit parameters of Z -sources Sco X-1 and GX 340+0 (1) and Atoll Sources GX 3+1 (2), 4U 1728-34 (3), 4U 1820-30 (4), 4U 1705-44 and “Atoll+ Z ” Source XTE J1701-462 (5)

Source Name	Alternative Name	Class ⁶	Distance, (kpc)	Presence of kHz QPO	kT_e , (keV)	$N_{comptb} L_{39}^{soft}/D_{10}^2$	kT_s (keV)	f
Sco X-1	V818 Sco	Z, Sp, B	2.8 (7)	+(8)	3-180	0.3-3.4	0.4-1.8	0.08-1
4U 1642-45	GX 340+0	Z, Sp, B	10.5 (9)	+(12)	3-21	0.08-0.2	1.1-1.5	0.01-0.5
4U 1744-26	GX 3+1	Atoll, Sp, B	4.5(10)	none(13)	2.3-4.5	0.04-0.15	1.16-1.7	0.2-0.9
4U 1728-34	GX 354-0	Atoll, Su, D	4.2-6.4(11)	+(14)	2.5-15	0.02-0.09	1.3	0.5-1
4U 1820-30	...	Atoll, Su, B	5.8-8 (15)	+(16)	2.9-21	0.02-0.14	1.1-1.7	0.2-1
XTE J1701-462	...	Atoll+Z, Su, D	8.8(17)	+(18)	1-2.7	...
4U 1705-44	...	Atoll, Sp, B	7.4 (19)	+(20)	2.7-100	0.01-0.08	1.1-1.5	0.2-1

References: (1) STF13; (2) ST12; (3) ST11; (4) TSF13; (5) LRH109; (6) Classification of the system in the various schemes (see text): Sp = supercritical, Su = subcritical, B = bulge, D = disk; (7) Bradshaw et al. (1999); (8) Zhang et al. (2006); (9) Fender & Henry (2000), Ford et al. (1998), Christian & Swank (1997); (10) Kuulkers & van der Klis (2000), Ford et al. (2000); (11) van Paradijs (1978); (12) Jonker et al. (1998); (13) Strohmayer (1998); (14) Titarchuk & Osherovich (1999); (15) Shaposhnikov & Titarchuk (2004); (16) Smale et al. (1997); (17) Lin et al. (2007), Lin et al. (2009); (18) Sanna et al. (2010); (19) Haberl & Titarchuk (1995); (20) BO02

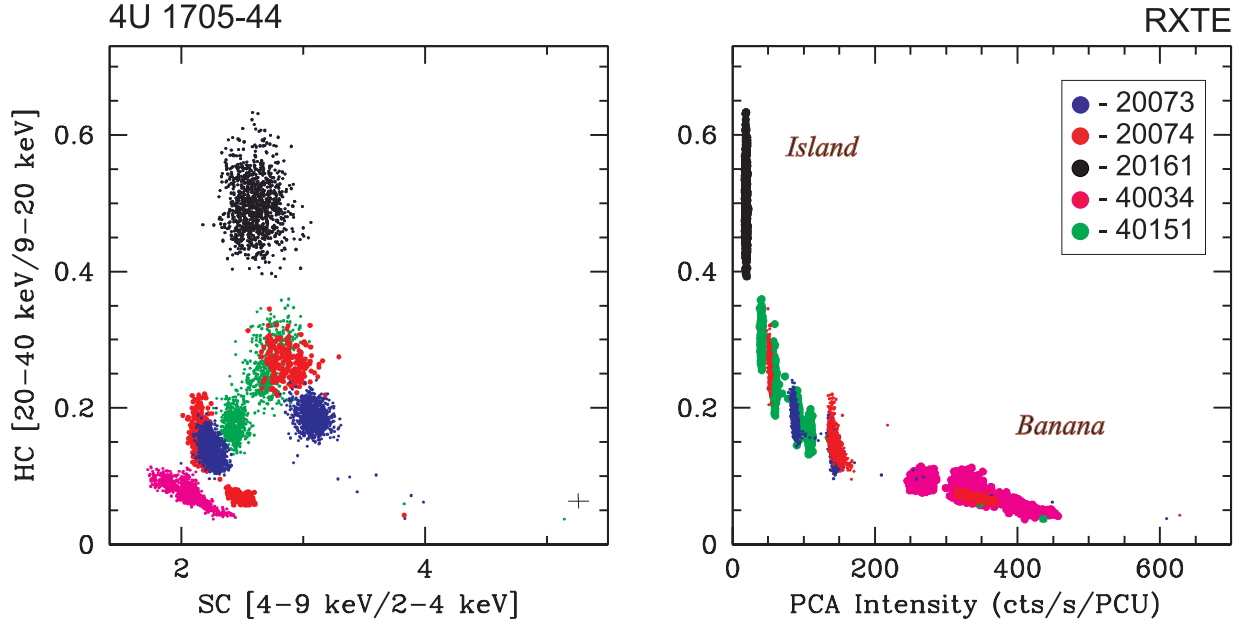


Fig. 2.— CDs (left) and HID (right) for all observations of 4U 1705-44 used in our analysis, with bin size 16 s. The typical error bars for the colors are shown in the bottom right corner of the left panel, while errors of the intensity are negligible. The sets are indicated by different colors: blue (ID 20073), red (ID 20074), black (ID 20161), crimson (ID 40034) and green (ID 40051).

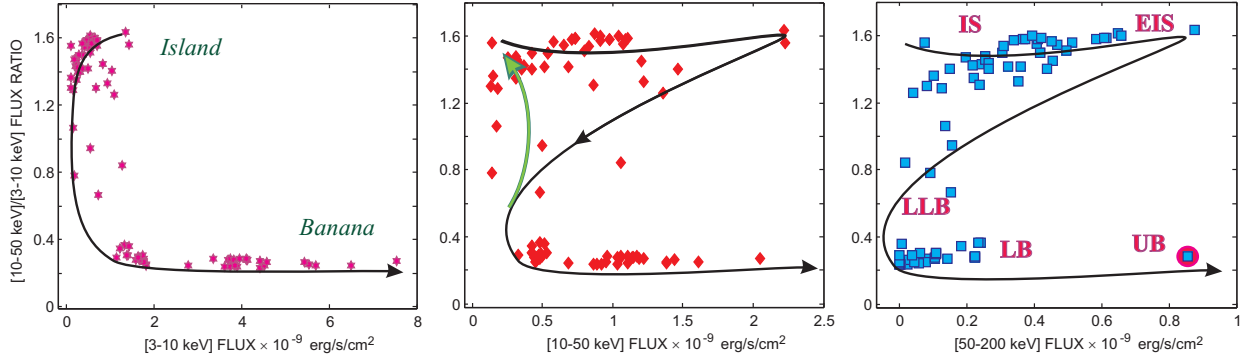


Fig. 3.— Left to right: flux ratio $[10-50 \text{ keV}/3-10 \text{ keV}]$ vs flux in $[3-10 \text{ keV}]$, $[10-50 \text{ keV}]$ and $[50-200 \text{ keV}]$ energy ranges measured in units of $10^{-9} \text{ erg s}^{-1} \text{ cm}^{-2}$. Black arrows indicate the direction of state changing from island to banana branches, while green arrow (middle panel) marks the direction of state changes from banana to island branch. In the right panel we indicate spectral states of 4U 1705-44 according to van Straaten (2000), and the point with pink oreole which spectrum is presented in Figure 7, related to “UB” state.

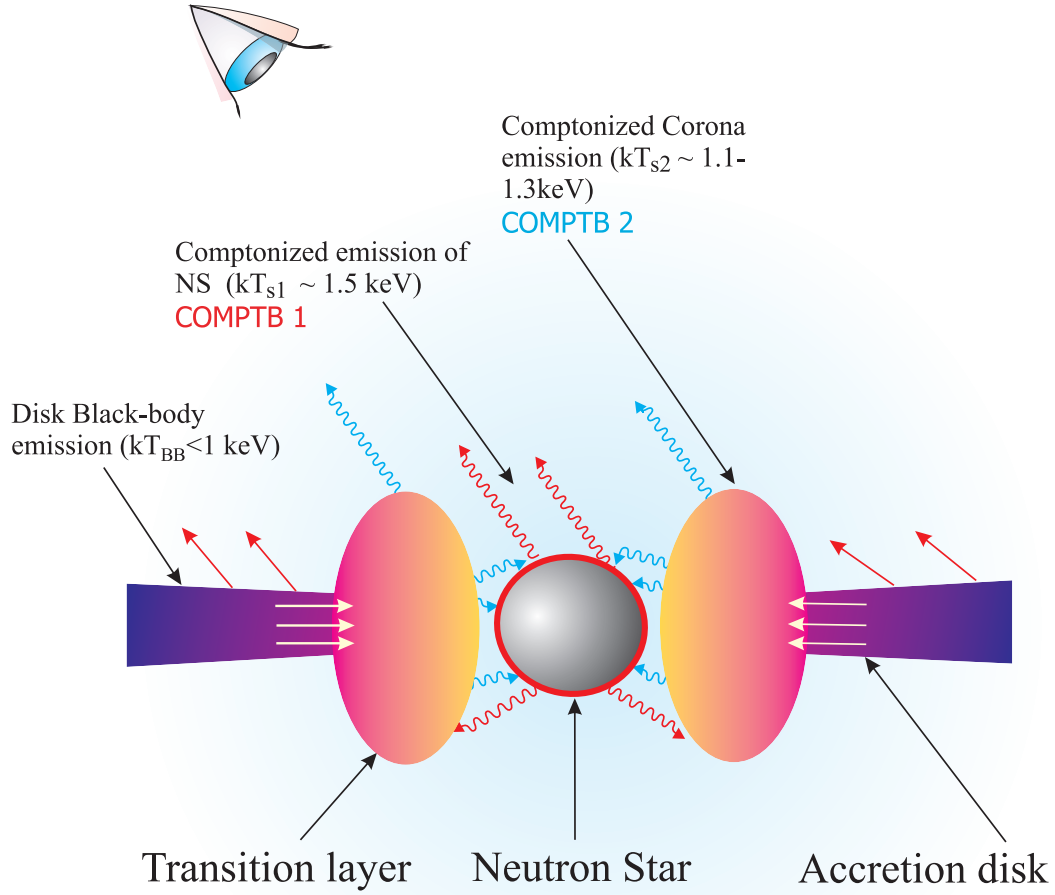


Fig. 4.— Suggested geometry of 4U 1705-44. Disk and NS soft photons are upscattered off hotter plasma of the transition Layer (TL) located between the accretion disk and NS surface. Some fraction of these photons is seen directly by the Earth observer. Red and blue photon trajectories correspond to soft and hard (upscattered) photons respectively. In our model two Comptonization components are considered. The first one (Comptb1) is associated with $T_{s1} \sim 1.5$ keV related to the NS surface while Comptb2 is related to the seed (disk) photon temperature, $T_{s1} = 1.1 - 1.3$ keV.

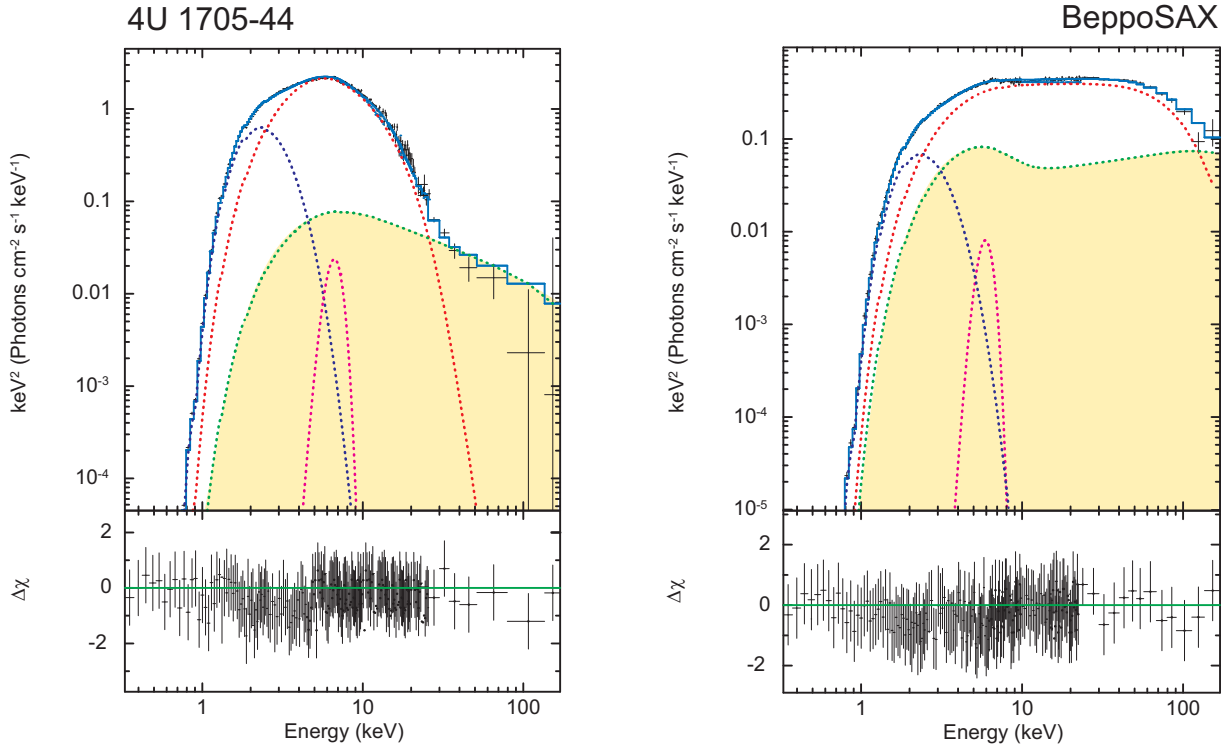


Fig. 5.— Two representative EF_E diagrams for banana and island state events of 4U 1705-44 using *BeppoSAX* data. Top: best-fit spectra of 4U 1705-44 in $E \cdot F(E)$ units using *BeppoSAX* observations 21292001 (left) and 21292002 (right). The data are presented by crosses, and the best-fit spectral model $wabs^*(blackbody+Comptb1+Comptb2+Gaussian)$ is presented by light-blue line. The model components are shown by dark blue, red, green and crimson lines for blackbody, Comptb1, Comptb2 and Gaussian components, respectively. Bottom panels: $\Delta\chi$ vs photon energy in keV. The best-fit model parameters for Banana state (left panel) are $\Gamma_1=1.99\pm0.02$, $kT_e^{(1)}=2.47\pm0.01$ keV, $\Gamma_2=2.00\pm0.01$, $kT_e^{(2)}=46.0\pm0.7$ keV and $E_{line}=6.95\pm0.04$ keV (reduced $\chi^2=1.07$ for 295 dof), while the best-fit model parameters for the island state (right panel) are $\Gamma_1=2.00\pm0.04$, $kT_e^{(1)}=18.9\pm0.2$ keV, $\Gamma_2=2.01\pm0.03$, $kT_e^{(2)}=51\pm1$ keV and $E_{line}=6.51\pm0.08$ keV (reduced $\chi^2=1.02$ for 296 dof) (see more details in Table 3).

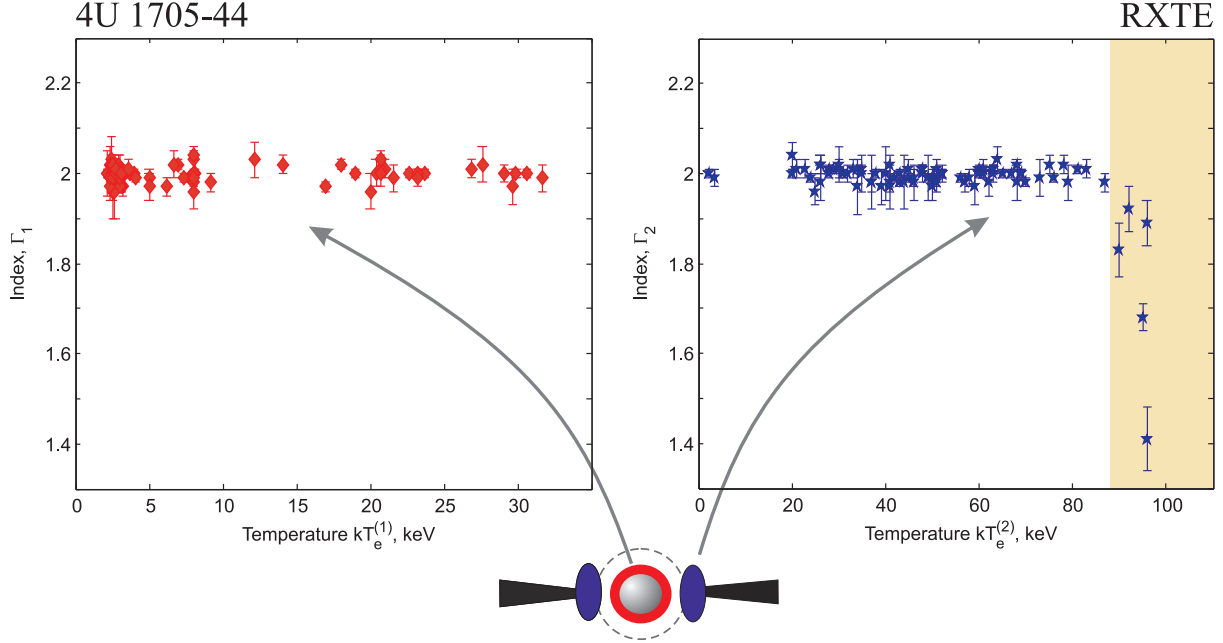


Fig. 6.— Photon indices Γ_1 and Γ_2 plotted vs. the best-fit electron temperatures of the Comptb1 and Comptb2 components, respectively, measured in keV (see Table 4). Red and blue points correspond to Comptb1 and Comptb2 components, which are related to thermal upscattering of soft photons by plasma electrons in the NS boundary layer and CC, respectively. The range of the high electron temperatures $kT_e^{(2)}$ where $\Gamma_2 < 2$ is shaded yellow.

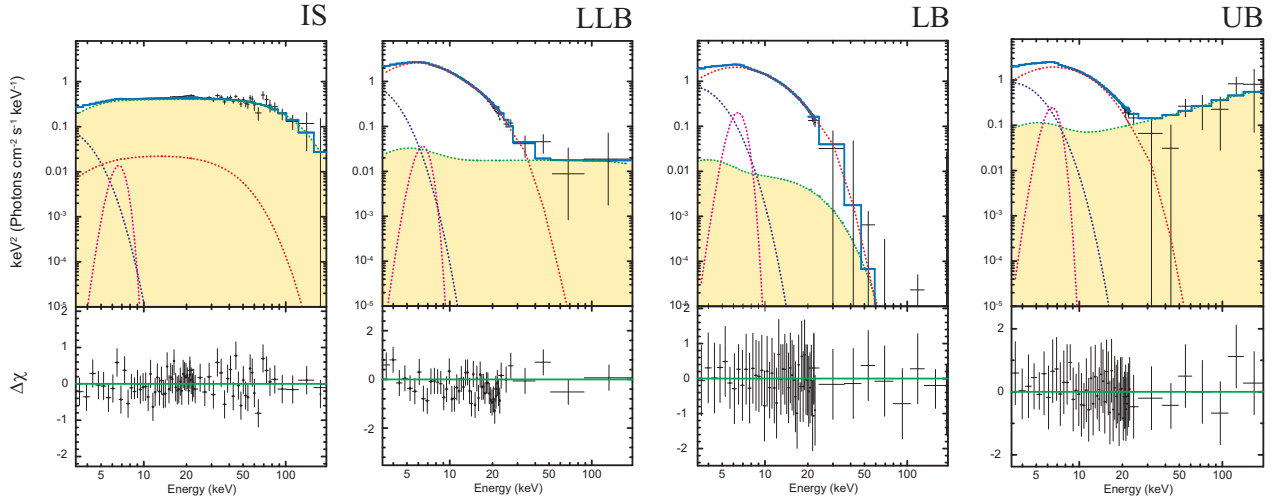


Fig. 7.— Four representative EF_E diagrams for different states along atoll-track of 4U 1705-44. Data are taken from *RXTE* observations 40034-01-09-00 (island state, IS), 40034-01-01-00 (lower left banana, LLB), 40034-01-02-09 (lower banana, LB), and 40034-01-02-06 (upper banana, UB). The data are shown by black crosses, and the spectral model components are displayed by dashed red, green, blue and purple lines for Comptb1, Comptb2, Blackbody and Gaussian, respectively. Yellow shaded areas reveal an evolution of Comptb2 component during the spectral transition (see also Figs. 2 and 6).

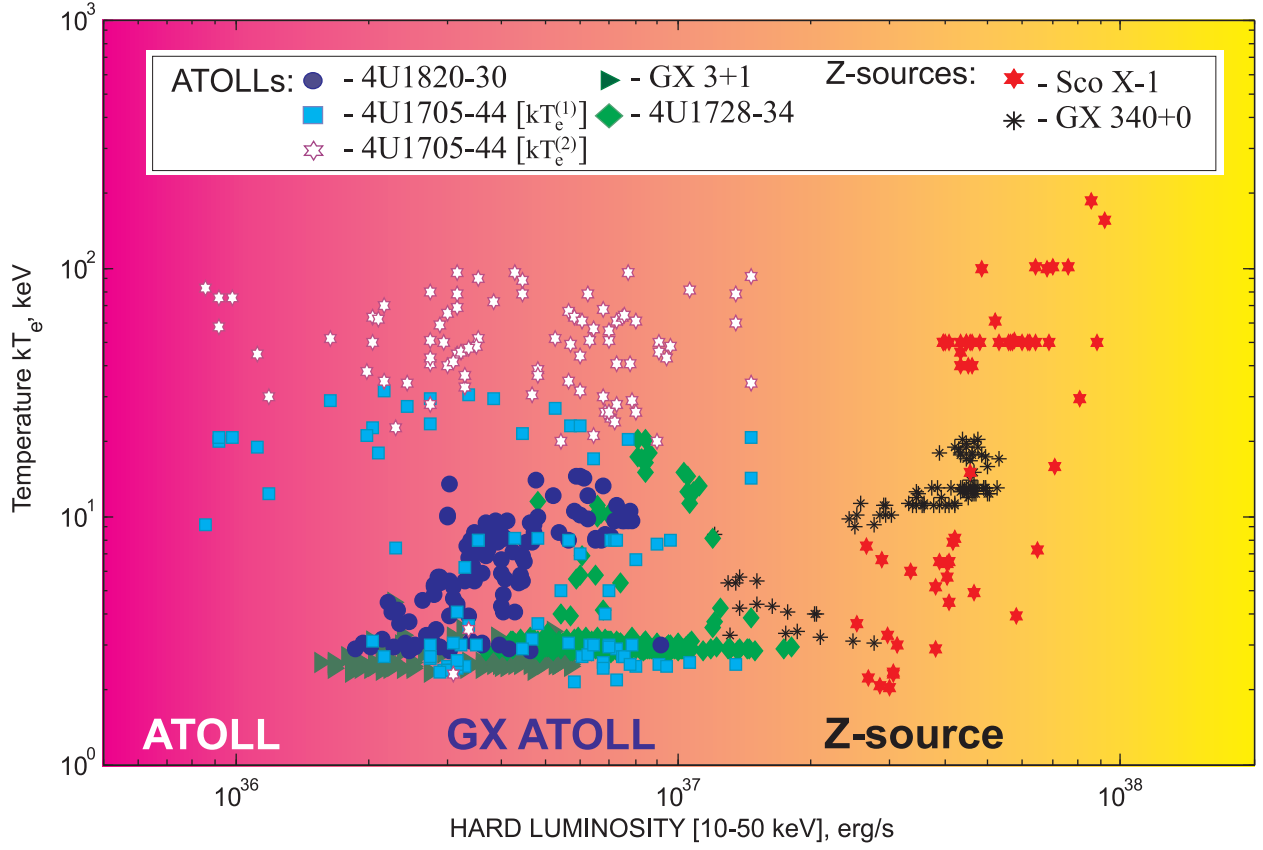


Fig. 8.— Electron temperature kT_e vs luminosity in the 10-50 keV range, using *RXTE* data for the Z-sources Sco X-1 (red; TSS14), GX 340+0 (black; STF13) and atolls 4U 1728-34 (bright green; ST11), GX 3+1 (dark green; ST12), 4U 1820-30 (dark blue; TSF13) and 4U 1705-44 [*light blue* ($kT_e^{(1)}$), *white* ($kT_e^{(2)}$)].

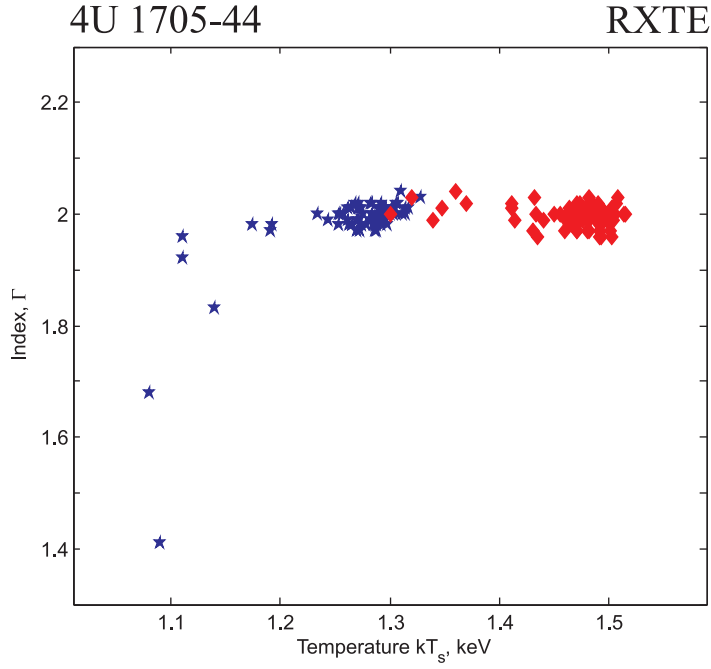


Fig. 9.— Photon indices Γ_1 and Γ_2 plotted vs. the seed photon temperatures of the Comptb1 and Comptb2 components, respectively, measured in keV. (see more details in Table 4). Red and blue points correspond to Comptb1 and Comptb2 components which are related to the Comptonization of the soft photons of the NS and disk by the electrons of the Compton cloud, respectively.

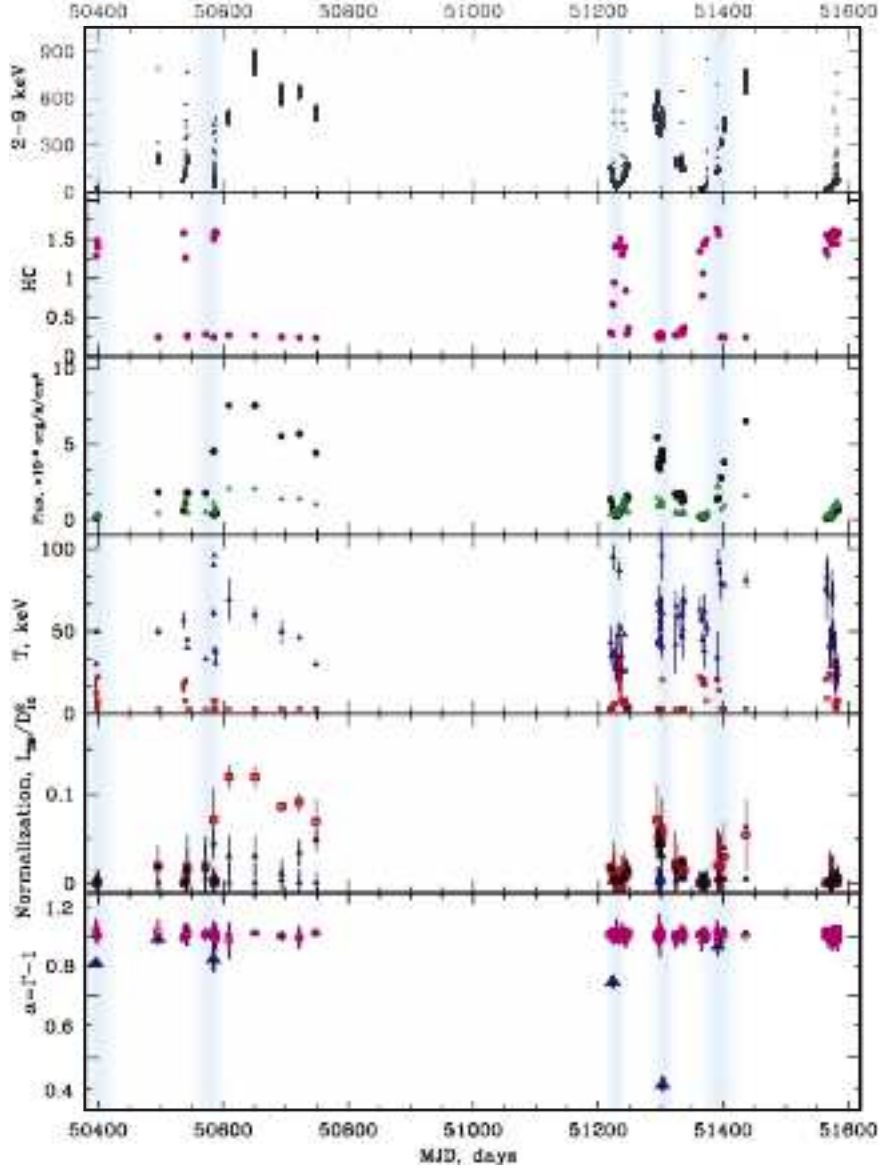


Fig. 10.— From Top to bottom: evolutions of count rate [2-9 keV] in counts s⁻¹ with 16 s time resolution, the hardness ratio coefficient HC [10-50 keV]/[3-10 keV], the model flux in the 3-10 keV and 10-50 keV energy ranges (black and green points, respectively), the electron temperatures $kT_e^{(1)}$ (red) and $kT_e^{(2)}$ (blue) in keV, blackbody normalizations of Comptb1 and Comptb2 (red and blue, respectively), and the spectral indices α_1 and α_2 (red and blue) for Comptb1 and Comptb2 components, respectively, for 1996–2000 evolution events (R1-R3 set). The phases of the light curve, related to the reduced spectral index α_2 , are marked with blue vertical strips.

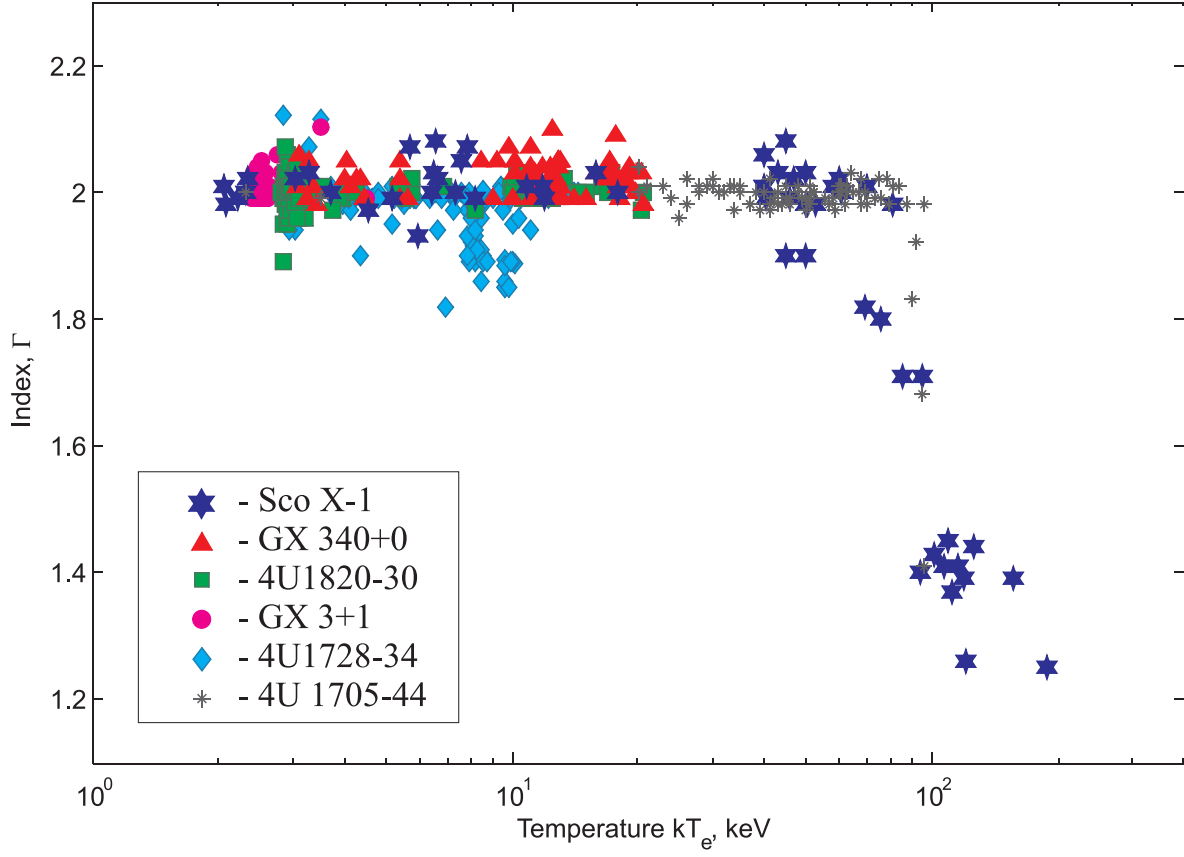


Fig. 11.— Photon index Γ vs. kT_e for Z -sources Sco X-1 (blue stars; TSS14) and GX 340+0 (red triangles; STF13) and atoll sources 4U 1705-44 (black), 4U 1728-34 (bright blue diamonds; ST11), GX 3+1 (pink circles; ST12), and 4U 1820-30 (green squares, TSF13).